Electronic Supplementary Material (ESI) for Physical Chemistry Chemical Physics.

Supplementary Information

Conor Jason Price,* Joe Pitfield, Edward Allery David Baker, and S. P. Hepplestone†

Department of Physics, University of Exeter,

Stocker Road, Exeter, EX4 4QL, United Kingdom

No. Intercalant Ions	Sites Filled	No. Intercalant Ions	Sites Filled
0	-	4	adeh
1	a	4	adfg
2	ab	4	adfh
2	ae	5	abcde
2	af	5	abcef
2	ah	5	abceh
3	abc	6	abcdef
3	abe	6	abcefg
3	bce	6	abdefg
4	abcd	6	bcdefg
4	abce	7	abcdefg
4	abch	8	abcdefgh

Table S I: Different intercalation configurations considered for both T and Hc phases.

I. STRUCTURAL DETAILS

A. Intercalation Configuration

As stated in the main article, the T-, Hc-, and α-phases of ScS_2 have been considered. The primitive unit cells of these phases are presented in Figure S1. The different structure of the T and H layers is in agreement with previous studies[1,2], as well as the α phase matching previous works[3,4]. For interalation, supercells of $(2 \times 2 \times 2)$ for the T-phase, $(2 \times 2 \times 1)$ for the Hc-phase, and $(2 \times 2 \times 1)$ for the α-phase were used for intercalation. For these supercell sizes, there were many symmetrically equivalent octahderal sites available for intercalation. For the T- and Hc-phases there are eight (8) different intercalation sites (indexed a-h), and for the α-phase there are twelve (12) different intercalation sites (indexed a-l). These sites are indicated with the green spheres in Figure S2. These different intercalation sites allow various symmetrically-unique configurations of intercalants which were each explored for obtaining the intercalation voltage. These configurations are presented in Table SI for the T- and Hc-phases and in Table SI for α-phases, where the sites occupied with an intercalant

No. Intercalant Ions	Sites Filled	No. Intercalant Ions	Sites Filled
0	-	8	bcegijkl
1	a	8	bcehijkl
4	abcd	8	bcfgijkl
4	abce	8	cdefhijk
4	abch	8	cdefhijl
4	abei	8	cdefhikl
4	abfi	8	cdefhjkl
4	abgi	8	cdeghjkl
4	abgj	8	cdfghjkl
4	abgk	8	defgijkl
4	abgl	8	dfghijkl
4	adeh	8	efghijkl
4	adfg	11	abcdefghijk
4	adfg	12	abcdefghijkl

Table S II: Different intercalation configurations considered for α phase.

are indicated with the letters (a-h) and (a-l). Due to the number of intercalation sites (and hence the number of intercalation configurations) for the α-phase, we have performed a more limited investigation across the intercalation range.

B. Lattice Constants

The real-space lattice constants for the different phases of ScS_2, intercalated with the different intercalants, obtained using the PBE functional in this work are presented in Table SIII. Where possible, lattice constants found within the literature have also been presented along with the source. We see that the calculated values are in very good agreement with the experimental values, being within 1%.

Material	a (Å)	c (Å)	c/a	Source
T-$LiScS_2$	3.610	6.135	1.699	This work
Hc-$LiScS_2$	3.569	12.409	3.477	This work
α-$LiScS_2$	3.652	17.910	4.904	This work
$LiScS_2$	3.687	18.318	4.968	van Dijk[3]
T-$NaScS_2$	3.694	6.736	1.824	This work
Hc-$NaScS_2$	3.638	13.553	3.725	This work
α-$NaScS_2$	3.732	19.467	5.216	This work
$NaScS_2$	3.751	19.744	5.264	van Dijk[3]
T-$KScS_2$	3.774	7.432	1.969	This work
Hc-$KScS_2$	3.701	15.151	4.093	This work
α-$KScS_2$	3.800	21.806	5.738	This work
$KScS_2$	3.814	21.726	5.697	Havlak[4]
$KScS_2$	3.811	21.719	5.700	Havlak[4]
T-$MgScS_2$	3.598	6.234	1.733	This work
Hc-$MgScS_2$	3.584	12.621	3.522	This work
α-$MgScS_2$	3.612	18.491	5.119	This work

Table S III: Lattice constants of the different phases of ScS_2 intercalated with different species.

Phase	Relative Energy of Intercalation Site	
	Octahedral (eV)	Tetrahedral (eV)
T	0	0.04
Hc	0	0.31
Tp	0	0.38

Table S IV: Relative energies for the different Li intercalation sites considered for T-, Hc-, and α-ScS_2 phases.

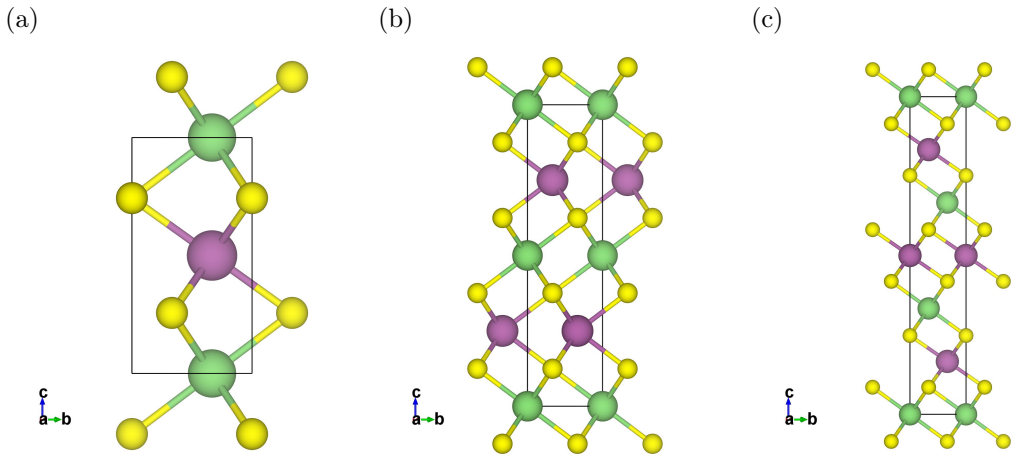

Figure S 1: Side-on views of each of the unit cells for the different phase of intercalated ScS_2 considered in this work. S1a shows the T-phase, S1b shows the Hc-phase, and S1c shows the α-phase.

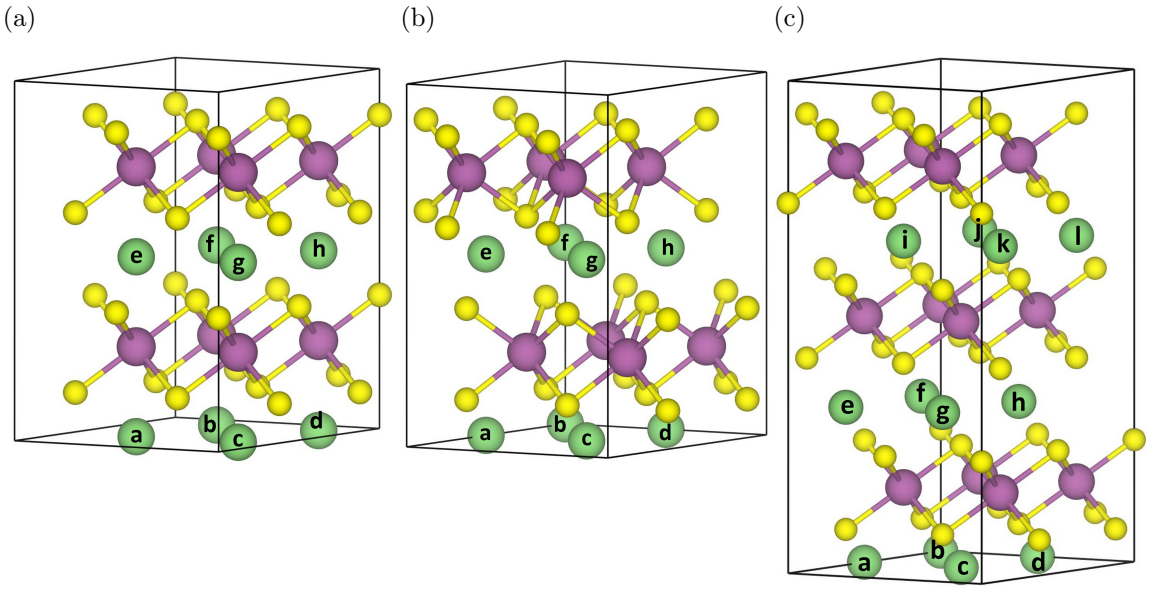

Figure S 2: The different intercalation sites available in the supercells of T- (S2a), Hc- (S2b), and α-ScS_2 (S2c) considered in this work.

C. Determining Intercalation Site

To determine the preferred site of intercalation, two different methods were explored. The first method was by intercalating at known interacalation sites for other TMDC structures

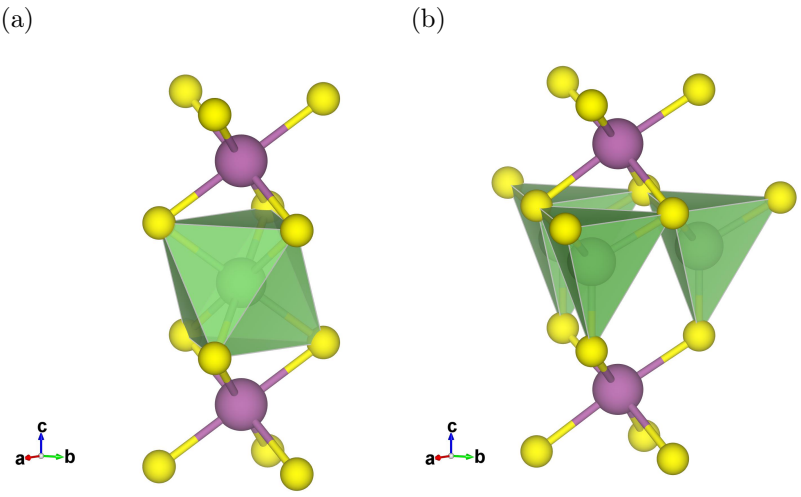

Figure S 3: Octahedral (S3a) and tetrahedral (S3b) coorindation of an intercalant with sulfur in intercalated ScS_2.

in the literature[5–9]. For the T- and H-phases, the intercalation sites considered were the octahedrally coordinated site above the scandium atom, and the tetrahedrally coordinated site above the chalcogen atom, labelled O and T, respectively. These are depicted in Figure S3. For α-ScS_2, the sites considered also have octahedral and tetrahedral coordination, but their positions with respect to the scandium atom are different due to the shift of the layers. Geometric relaxations were performed on these to obtain the relative energy of the two sites. The data for this is presented in Table SIV, where for all three phases it can be seen that the octahedral site is lowest in energy (due to the higher Li-S coordination).

To ensure a more thorough exploration of the potential intercalation sites, nudged elastic band (NEB) methods, as employed in VASP, were used to consider transition states for lithium diffusion through the system[10,11] (using the PBE functional). This method uses a series of interpolated 'images' along a specified path to determine the activation energies for diffusion. The initially interpolated images along the reaction pathway were relaxed according to the NEB method, converging the force with a tolerance of 0.1 eV/Å.

NEB calculations were performed along three different routes between two intercalation sites in bilayer systems with fixed positions of the scandium atoms, for each of the phases considered, using lithium as the intercalant. The NEB routes between two equivalent O sites (Route A), between adjacent O and T sites (Route B) and between two equivalent T sites (Route C) were considered, and are shown in Figure S4b for the T-phase and Figure S4d for

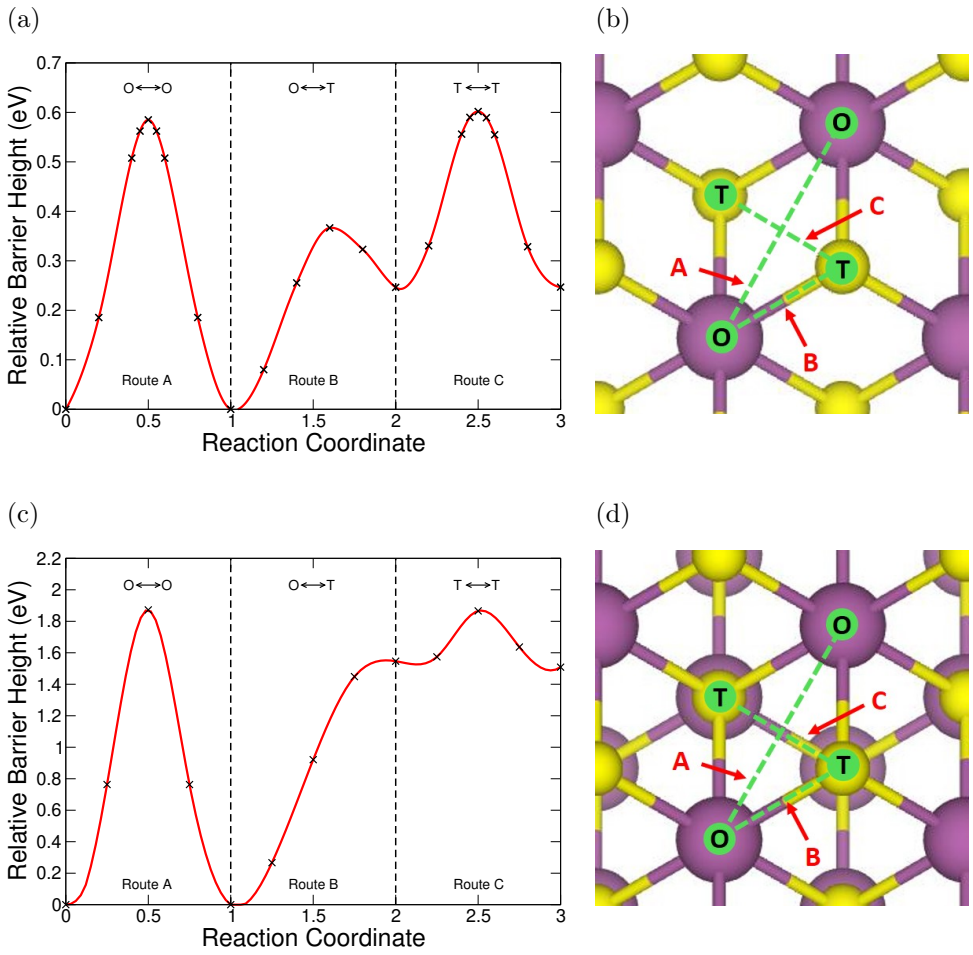

Figure S 4: Nudged elastic band results used to determine site of intercalation. S4a shows the results for T-ScS_2 along the routes presented in S4b. Similarly, S4c shows the results for α-ScS_2 along the routes presented in S4d. The intercalation sites these routes are between, the octahedrally coordinated (O) and tetrahedrally coordinated (T), are also indicated.

the α-phase. These results again show that the most favourable intercalation site for each of the phases is the octahedral-coordination (O) site. This is in agreement with other TMDC works[5–8], as well as the results of the structure search.

II. ELASTIC PROPERTIES

A. Bulk Moduli

The bulk modulus has been calculated by applying a uniform strain and compression of the unit cells (i.e. equally along the three axis directions). The resultant graphs of energy as a function of volume are then fitted with a parabolic curve, which can then be used in $B = V_0 \frac{\partial^2 E}{\partial V^2}$ to obtain the bulk modulus. The obtained plots of energy with volume, as well as the resulting values for the bulk modulus, are presented in Figure S5.

B. Elastic Tensor

An alternative, more rigorous treatment involves the calculation of the elastic tensor. Using the elements of the elastic tensor, different elastic moduli can be determined. We employ different schemes to obtain the bulk (B) and shear (G) moduli, from which many other elastic properties can be determined[12]. Upper bounds of these quantities, denoted B_V and G_V, can be found using the Voigt scheme, with the bulk modulus being given by,

$$\begin{aligned} B_V &= \frac{1}{9}\big[(c_{11} + c_{22} + c_{33}) + 2(c_{12} + c_{23} + c_{31})\big] \\ G_V &= \frac{1}{15}\big[(c_{11} + c_{22} + c_{33}) - (c_{12} + c_{23} + c_{31}) + 3(c_{44} + c_{55} + c_{66})\big]. \end{aligned} \tag{S1}$$

Alternatively, we can use the Reuss scheme to obtain the lower bounds of B_R and G_R,

$$\begin{aligned} \frac{1}{B_R} &= (S_{11} + S_{22} + S_{33}) + 2(S_{12} + S_{23} + S_{31}) \\ \frac{1}{G_R} &= \frac{1}{15}\big[4(S_{11} + S_{22} + S_{33}) - 4(S_{12} + S_{23} + S_{31}) + 3(S_{44} + S_{55} + S_{66})\big]. \end{aligned} \tag{S2}$$

The results of the Voigt and Reuss schemes can be combined in the Voigt-Reuss-Hill scheme, where an average of the upper (V) and lower (R) bounds is taken,

$$\begin{aligned} B_{VRH} &= \frac{B_V + B_R}{2} \\ G_{VRH} &= \frac{G_V + G_R}{2}. \end{aligned} \tag{S3}$$

A geometric mean has also been used in some works[12].

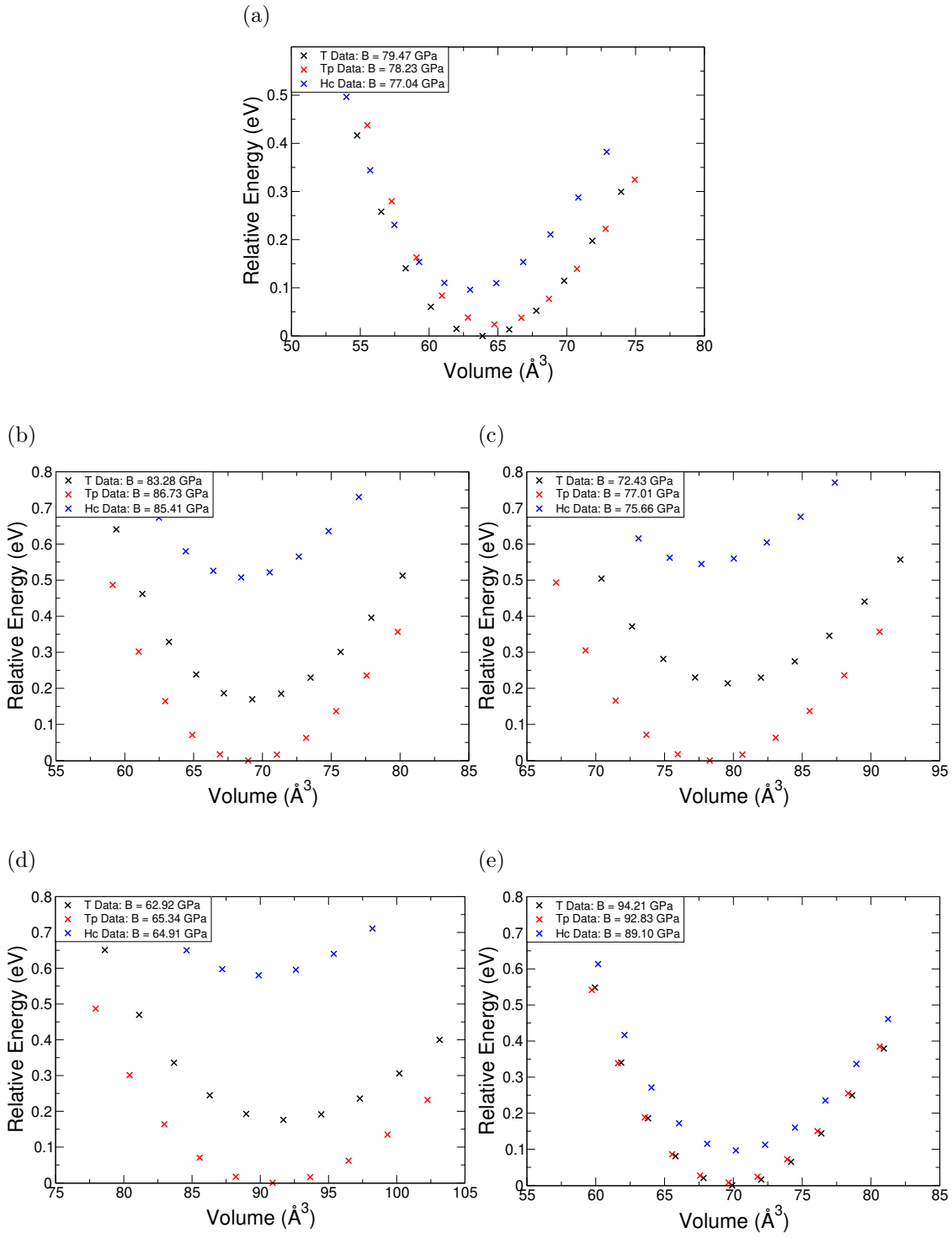

Figure S 5: Energy of materials with varied volume. S5a presents the data for pristine ScS_2, and S5b, S5c, S5d, and S5e present the data for lithium, sodium, potassium, and magnesium respectively. Each has been normalised to be energy and volume per formula unit, and scaled so that the lowest energy is set to zero. The resulting bulk modulus (B) is included in each subfigure.

	c_{ij}						B (GPa)	G (GPa)	Y (GPa)	ν	R
T-ScS_2	80.33	33.10	18.82	−1.32	0.00	0.00	V: 37.62 R: 30.87 Av: 34.25	V: 10.16 R: -43.31 Av: -16.57	V: 27.97	V: 0.38	V: 3.70
		80.33	18.82	1.32	0.00	0.00					
			36.48	0.00	0.00	0.00					
				−7.47	0.00	0.00					
					−7.47	−1.32					
						23.62					

Table S V: Elastic properties for pristine T-ScS_2. The elastic tensor elements (c_{ij}) were used to obtain the bulk modulus (B), shear modulus (G), and Young's modulus (Y). The Poisson ratio (ν), and the Pugh ratio (R) are also given. The Voigt (V), Reuss (R), and VRH (Av) values have been included for the bulk and shear moduli.

$$\begin{aligned} B_{GM} &= \sqrt{B_V B_R} \\ G_{GM} &= \sqrt{G_V G_R}. \end{aligned} \tag{S4}$$

From these, the Young's modulus, Y, the Poisson ratio, ν, and the Pugh ratio, R, can be obtained:

$$\begin{aligned} \mathrm{Y} &= \frac{9\mathrm{BG}}{3\mathrm{B}+\mathrm{G}} \\ \nu &= \frac{3\mathrm{B}-2\mathrm{G}}{2(3\mathrm{B}+\mathrm{G})} \\ \mathrm{R} &= \frac{\mathrm{B}}{\mathrm{G}}. \end{aligned} \tag{S5}$$

Whilst the values for the bulk modulus of the T-phase ScS_2 compounds calculated using the elastic tensor (given in Table SV and Table SVI) are lower than those presented in Figure S5, those obtained using the elastic tensor allow for ionic relaxation, whereas those obtained in Figure S5 did not. We also present in Table SVII and Table SVIII the same data for the α-phase.

We are also able to comment on the elastic stability of these materials. Rhombohedral crystals have elastic tensors of the form,

	c_{ij}						B (GPa)	G (GPa)	Y (GPa)	ν	R
T-$LiScS_2$	141.15	40.71	16.28	5.40	0.00	0.00	V: 60.22 R: 58.02 Av: 59.20	V: 42.46 R: 37.82 Av: 40.11	V: 103.14 R: 93.20 Av: 98.16	V: 0.21 R: 0.23 Av: 0.22	V: 1.42 R: 1.53 Av: 1.48
		141.15	16.28	−5.40	0.00	0.00					
			110.96	0.00	0.00	0.00					
				27.89	0.00	0.00					
					27.89	5.40					
						50.22					
T-$NaScS_2$	118.16	37.56	19.70	−2.84	0.00	0.00	V: 54.45 R: 53.39 Av: 53.94	V: 34.54 R: 31.27 Av: 32.89	V: 85.53 R: 78.50 Av: 82.00	V: 0.23 R: 0.25 Av: 0.25	V: 1.58 R: 1.71 Av: 1.64
		118.16	19.70	2.84	0.00	0.00					
			99.78	0.00	0.00	0.00					
				23.01	0.00	0.00					
					23.01	−2.84					
						40.30					
T-$KScS_2$	97.68	32.11	21.84	−7.18	0.00	0.00	V: 50.18 R: 50.18 Av: 50.18	V: 30.65 R: 27.27 Av: 28.96	V: 76.39 R: 69.25 Av: 72.85	V: 0.25 R: 0.28 Av: 0.26	V: 1.64 R: 1.84 Av: 1.73
		97.68	21.84	7.18	0.00	0.00					
			104.73	0.00	0.00	0.00					
				22.84	0.00	0.00					
					22.84	−7.18					
						32.78					
T-$MgScS_2$	157.67	49.81	56.05	6.78	0.00	0.00	V: 91.99 R: 91.13 Av: 91.61	V: 59.48 R: 58.35 Av: 58.42	V: 146.79 R: 144.26 Av: 144.53	V: 0.23 R: 0.24 Av: 0.24	V: 1.55 R: 1.56 Av: 1.57
		157.67	56.05	6.78	0.00	0.00					
			188.68	0.00	0.00	0.00					
				64.71	0.00	0.00					
					64.71	6.78					
						53.93					

Table S VI: Elastic properties for each of the intercalated T-ScS_2 structures. The elastic tensor elements (c_{ij}) were used to obtain the bulk modulus (B), shear modulus (G), and Young's modulus (Y). The Poisson ratio (ν), and the Pugh ratio (R) are also given. The Voigt (V), Reuss (R), and VRH (Av) values have each been included.

	c_{ij}						B (GPa)	G (GPa)	Y (GPa)	ν	R
α-ScS_2	69.64	36.67	27.91	7.78	0.00	0.00	V: 37.96 R: 9.85 Av: 23.90	V: -2.77 R: 6.06 Av: 1.65	R: 15.09	R: 0.24	R: 1.62
		69.64	27.91	−7.78	0.00	0.00					
			17.38	0.00	0.00	0.00					
				−25.85	0.00	0.00					
					−25.85	7.78					
						16.48					

Table S VII: Elastic properties for pristine α-ScS_2. The elastic tensor elements (c_{ij}) were used to obtain the bulk modulus (B), shear modulus (G), and Young's modulus (Y). The Poisson ratio (ν), and the Pugh ratio (R) are also given. The Voigt (V), Reuss (R), and VRH (Av) values have been included for the bulk and shear moduli.

$$\begin{pmatrix} c_{11} & c_{12} & c_{13} & c_{14} & & \\ \cdot & c_{11} & c_{13} & -c_{14} & & \\ \cdot & \cdot & c_{33} & & & \\ \cdot & \cdot & & c_{44} & & \\ & & & & c_{44} & c_{14} \\ & & & & \cdot & c_{66} \end{pmatrix}, \tag{S6}$$

which matches the form of the elastic tensors determined for the materials considered here. To ensure elastic stability, there are certain conditions that are necessary to be met[13], namely,

1. $c_{11} > |c_{12}|$
2. $c_{44} > 0$
3. $c_{13}^2 < \frac{1}{2}c_{33}(c_{11} + c_{12})$
4. $c_{14}^2 < \frac{1}{2}c_{44}(c_{11} - c_{12}) = c_{44}c_{66}$.

From the data presented in the above tables, it is found that each of the intercalated structures satisfies all of these conditions. However, the pristine ScS_2 structures (both T and α-phases) do not meet conditions 2 and 4, due to the negative values of the c_{44} elements.

	c_{ij}						B (GPa)	G (GPa)	Y (GPa)	ν	R
α-$LiScS_2$	142.65	36.92	32.74	−1.07	0.00	0.00	V: 66.97 R: 66.02 Av: 66.49	V: 43.92 R: 42.10 Av: 43.01	V: 108.12 R: 104.17 Av: 106.15	V: 0.23 R: 0.24 Av: 0.23	V: 1.52 R: 1.57 Av: 1.55
		142.65	32.74	1.07	0.00	0.00					
			112.61	0.00	0.00	0.00					
				34.11	0.00	0.00					
					34.11	−1.07					
						52.87					
α-$NaScS_2$	125.28	32.81	32.32	7.95	0.00	0.00	V: 60.45 R: 59.72 Av: 60.08	V: 40.25 R: 38.36 Av: 39.31	V: 98.82 R: 94.79 Av: 96.81	V: 0.23 R: 0.24 Av: 0.23	V: 1.50 R: 1.56 Av: 1.53
		125.28	32.32	−7.95	0.00	0.00					
			98.58	0.00	0.00	0.00					
				35.57	0.00	0.00					
					35.57	7.95					
						46.23					
α-$KScS_2$	101.36	28.46	29.46	10.56	0.00	0.00	V: 53.47 R: 53.46 Av: 53.47	V: 34.88 R: 32.06 Av: 33.46	V: 85.94 R: 80.15 Av: 83.07	V: 0.23 R: 0.25 Av: 0.24	V: 1.53 R: 1.67 Av: 1.60
		101.36	29.46	−10.56	0.00	0.00					
			103.76	0.00	0.00	0.00					
				32.45	0.00	0.00					
					32.45	10.56					
						36.45					
α-$MgScS_2$	165.39	49.00	58.22	17.48	0.00	0.00	V: 91.12 R: 91.12 Av: 91.12	V: 60.71 R: 56.28 Av: 58.49	V: 149.02 R: 140.02 Av: 144.55	V: 0.23 R: 0.24 Av: 0.24	V: 1.50 R: 1.62 Av: 1.56
		165.39	58.22	−17.48	0.00	0.00					
			158.47	0.00	0.00	0.00					
				68.70	0.00	0.00					
					68.70	17.48					
						58.20					

Table S VIII: Elastic properties for each of the intercalated α-ScS_2 structures. The elastic tensor elements (c_{ij}) were used to obtain the bulk modulus (B), shear modulus (G), and Young's modulus (Y). The Poisson ratio (ν), and the Pugh ratio (R) are also given. The Voigt (V), Reuss (R), and VRH (Av) values have each been included.

III. PHASE DIAGRAMS

A. Derivation

For ScS_2 intercalated with some amount a of a metal M, be that a Group I metal (in the following example we use Li) or a Group II metal (in the following example we use Mg), we define the enthalpy of formation of relevant products:

$$\Delta H(\mathrm{Li_aScS_2}) = E(\mathrm{Li_aScS_2}) - [a\mu^0_{Li} + \mu^0_{Sc} + 2\mu^0_S] \tag{S7}$$

$$\Delta H(\mathrm{ScS_2}) = E(\mathrm{ScS_2}) - [\mu^0_{Sc} + 2\mu^0_S] \tag{S8}$$

$$\Delta H(\mathrm{Li_2S}) = E(\mathrm{Li_2S}) - [2\mu^0_{Li} + \mu^0_S] \tag{S9}$$

$$\Delta H(\mathrm{MgS}) = E(\mathrm{MgS}) - [\mu^0_{Mg} + \mu^0_S] \tag{S10}$$

where $\Delta H(A)$ gives the enthalpy of formation of the compound A, $E(A)$ gives the energy of the compound A, and $\mu^0_B = E(B)$ gives the chemical potential of elemental species B when it is in its elemental bulk structure.

The thermodynamic equilibrium condition requires,

$$\Delta H(\mathrm{Li_aScS_2}) = a\Delta\mu_{Li} + \Delta\mu_{Sc} + 2\Delta\mu_S, \tag{S11}$$

where we have used the notation $\Delta\mu_B = \mu_B - \mu^0_B$, with μ_B being the chemical potential of elemental species B in $\mathrm{Li_aScS_2}$. This simply states that the energy of the intercalated structure is the sum of the chemical potentials of the constituent atoms. Rearranging the thermodynamic equilibrium condition gives,

$$\Delta\mu_S = \frac{1}{2}\big\{\Delta H(\mathrm{Li_aScS_2}) - [a\Delta\mu_{Li} + \Delta\mu_{Sc}]\big\}. \tag{S12}$$

We require that ScS_2, Li_2S, MgS, and the bulk forms of the component elements do not form. Therefore,

$$\Delta\mu_{Sc} + 2\Delta\mu_S \leq \Delta H(\mathrm{ScS_2}), \tag{S13}$$

$$2\Delta\mu_{Li} + \Delta\mu_S \leq \Delta H(\mathrm{Li_2S}), \tag{S14}$$

$$\Delta\mu_{Mg} + \Delta\mu_S \leq \Delta H(\mathrm{MgS}), \tag{S15}$$

$$\Delta\mu_{Li,Mg,Sc,S} \leq 0. \tag{S16}$$

Substituting (S12) into (S13) and rearranging,

$$\frac{1}{a}\big[\Delta H(\mathrm{Li_aScS_2}) - \Delta H(\mathrm{ScS_2})\big] \leq \Delta\mu_{Li}. \tag{S17}$$

This then gives our first thermodynamic limit on the lithium chemical potential such that the intercalation of the layered ScS_2 structure is preferred to the pristine ScS_2 structure and bulk lithium.

We now substitute (S12) into (S14), and rearranging gives,

$$\Delta\mu_{Li} \leq \frac{1}{4-a}\big[2\Delta H(\mathrm{Li_2S}) - \Delta H(\mathrm{Li_aScS_2}) + \Delta\mu_{Sc}\big]. \tag{S18}$$

This gives the limit on the chemical potential of lithium such that the product Li_2S, an experimentally observed product of the conversion reaction of lithium with TMDC sulfides, does not form. We similarly substitute (S12) into (S15), giving,

$$\Delta\mu_{Mg} \leq \frac{1}{2-a}\big[2\Delta H(\mathrm{MgS}) - \Delta H(\mathrm{Mg_aScS_2}) + \Delta\mu_{Sc}\big]. \tag{S19}$$

The above equations thus describe the boundary conditions for the chemical potential of an intercalated metal, dependent on formation energies of the relevant products, and the chemical potentials of the relevant metals. It should be noted, by considering the equations (S7)-(S10), that the limiting conditions for both the single TMDC and superlattice, equations (S16)-(S19), are independent of μ_S^0, and hence $\Delta\mu_S$. As a result, the phase diagrams are only dependent on the chemical potentials of the intercalated species and the relevant metals, $\Delta\mu_{Li}$, $\Delta\mu_{Mg}$, and $\Delta\mu_{Sc}$.

Using equations (S16), (S17) and (S18)/(S19), we can construct thermodynamic phase diagrams, and a schematic of one is shown in Figure 2c of the main article. We restrict ourselves to the negative-negative quadrant to ensure that the elemental bulks do not form (equation (S16)). Above the diagonal line, labelled "1", the experimentally observed Li_2S crystal is favoured, as opposed to the intercalated ScS_2. Below the horizontal line, labelled "2", the pristine ScS_2 structure is preferred to intercalation. From this, we show intercalation is favoured for chemical potential combinations that sit within the shaded region indicated in Figure 2c of the main article. Outside of this window, however, the secondary products (as indicated in the figure) are favourable to form. Though a transition to these is not guaranteed, the intercalated ScS_2 structure becomes meta-stable. Whilst other compounds could have their respective boundaries determined to be included in these phase diagrams, such as (for the case of lithium intercalation) Li_2S_2 or ScS, these first require the disintegration of the Li_aScS_2 material into Li_2S and/or elemental bulks. Hence, we only consider the limits outlined above.

To quantitatively compare the phase diagrams for the different concentrations considered, we can evaluate the difference between the intercepts of lines 1 and 2 with the $\Delta\mu_{Li}$-axis. E_{IS} is then defined as,

$$E_{IS} = \Delta\mu_{Li}^{(1)}(\Delta\mu_{Sc} = 0) - \Delta\mu_{Li}^{(2)}(\Delta\mu_{Sc} = 0), \tag{S20}$$

where $\Delta\mu_{Li}^{(1/2)}(\Delta\mu_{Sc} = 0)$ is the value of the boundary line 1/2 at the point where $\Delta\mu_{Sc} = 0$. For lithium intercalation, using (S17) and (S18) this can be written in terms of the relevant values for formation enthalpy,

$$E_{IS}^{Li} = \frac{2}{4-a}\Delta H(\mathrm{Li_2S}) + \frac{1}{a}\Delta H(\mathrm{ScS_2}) - \frac{4}{4a-a^2}\Delta H(\mathrm{Li_aScS_2}), \tag{S21}$$

and for magnesium intercalation, using (S17) and (S19) this can be written as,

$$E_{IS}^{Mg} = \frac{2}{2-a}\Delta H(\mathrm{MgS}) + \frac{1}{a}\Delta H(\mathrm{ScS_2}) - \frac{2}{2a-a^2}\Delta H(\mathrm{Mg_aScS_2}). \tag{S22}$$

Each of the enthalpy of formation values should be negative for them to be thermodynamically stable with respect to their atomic constituents. When the value of E_{IS} is negative, the first two terms dominate, and line "1" intercepts below line "2" so no stability region exists. When the value of E_{IS}^{Li} is positive, however, $\Delta H(\mathrm{Li_aScS_2})$ dominates and the intercalated ScS_2 material is stable.

Using a similar set of arguments, we can construct equivalent phase diagrams for the systems where transition metal atoms substitutionally replace the scandium atoms of the host ScS_2 structure. Hence, we can also obtain an expression for E_{IS}, as,

$$E_{IS}^{Li} = \frac{2}{4-a}\Delta H(\mathrm{Li_2S}) + \frac{1}{a}\Delta H(\mathrm{MSS}) - \frac{4}{4a-a^2}\Delta H(\mathrm{LMMS}). \tag{S23}$$

Again, $\Delta H(A)$ gives the enthalpy of formation of the compound A, where MSS indicates the compound $\mathrm{M_bSc_{1-b}S_2}$, where metal M has replaced some proportion of scandium, and LMSS the intercalated MSS compound $\mathrm{Li_aM_bSc_{1-b}S_2}$. The similarity with equation (S21) is evident.

B. Phase Diagrams for Other ScS_2 Phases and Intercalants

We have evaluated phase diagrams for each of the intercalants for each of the phases of ScS_2 considered, in addition to the α-phase considered in the main article. Figures S6, S7 and S8 presents the data for intercalated T-ScS_2, Hc-ScS_2, and α-ScS_2 respectively. Each of the phases demonstrates a high value of E_{IS} for a range of intercalation concentrations. We note that for the Group I intercalants, all values exceed 2 eV, which are remarkably high compared to other TMDC materials. For Mg intercalation, there is a significant drop off in the values of E_{IS} for intercalant concentrations greater than $\mathrm{Mg_{0.5}ScS_2}$. This is due to the double valency of magnesium.

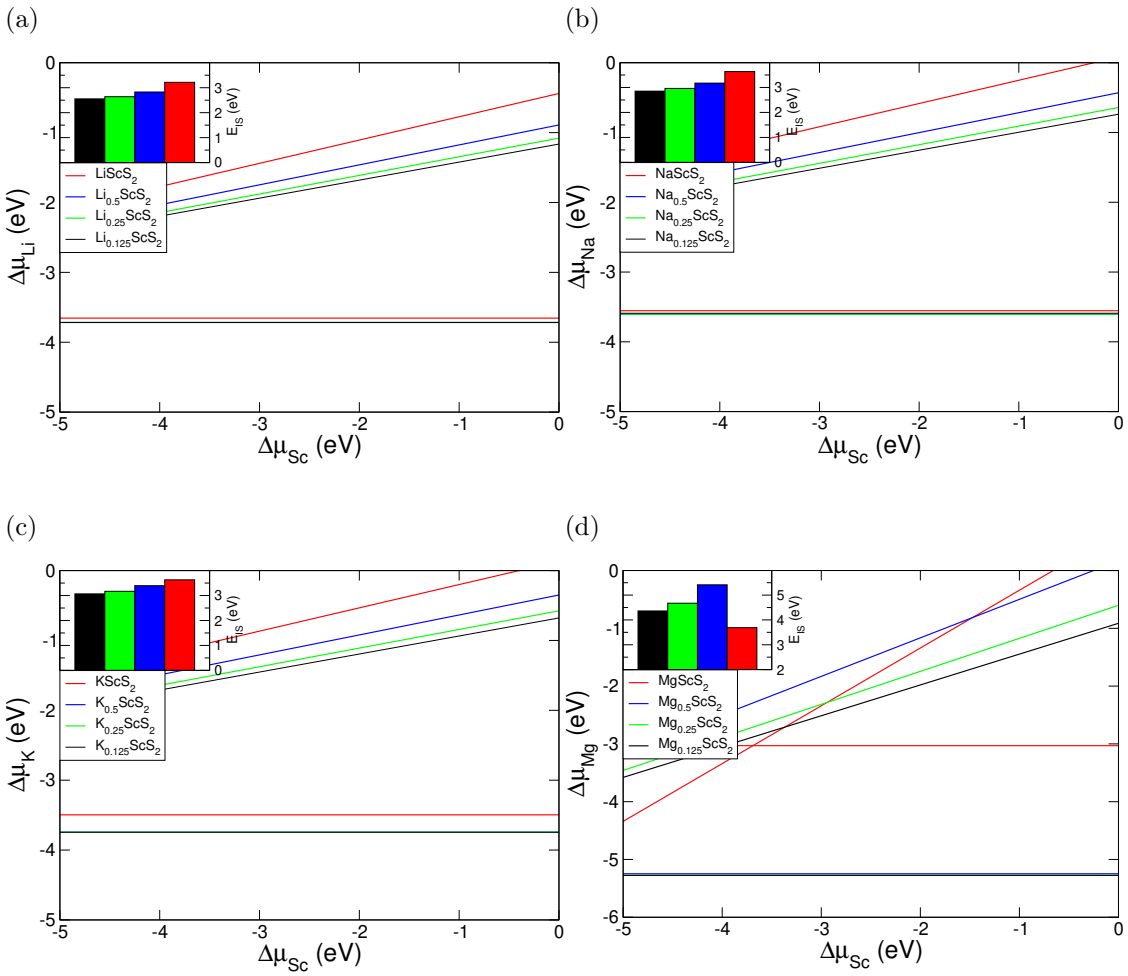

Figure S 6: S6a, S6b, S6c, and S6d show the phase diagrams for T-ScS_2 intercalated with different concentrations of Li, Na, K and Mg, respectively. The insets show the corresponding values of E_{IS}.

C. Additional Considerations for E_{IS}

The definition of E_{IS} in the main article does not account for the limits imposed by the bulk species. The lines defined by equations (S18) and (S19), and presented in Figures S6-S8, may cross above $\Delta\mu_M = 0$. This violates the condition given by equation (S16) requiring that the elemental bulk form of the intercalant species does not form. As such, the values of E_{IS} presented in the insets of Figures S6, S7, and S8 are optimistic and require correction. These adjusted values are presented in Table SIX. It is clear to see that the corrected values of E_{IS} are still remarkably large, and so the conclusions presented in the main article hold.

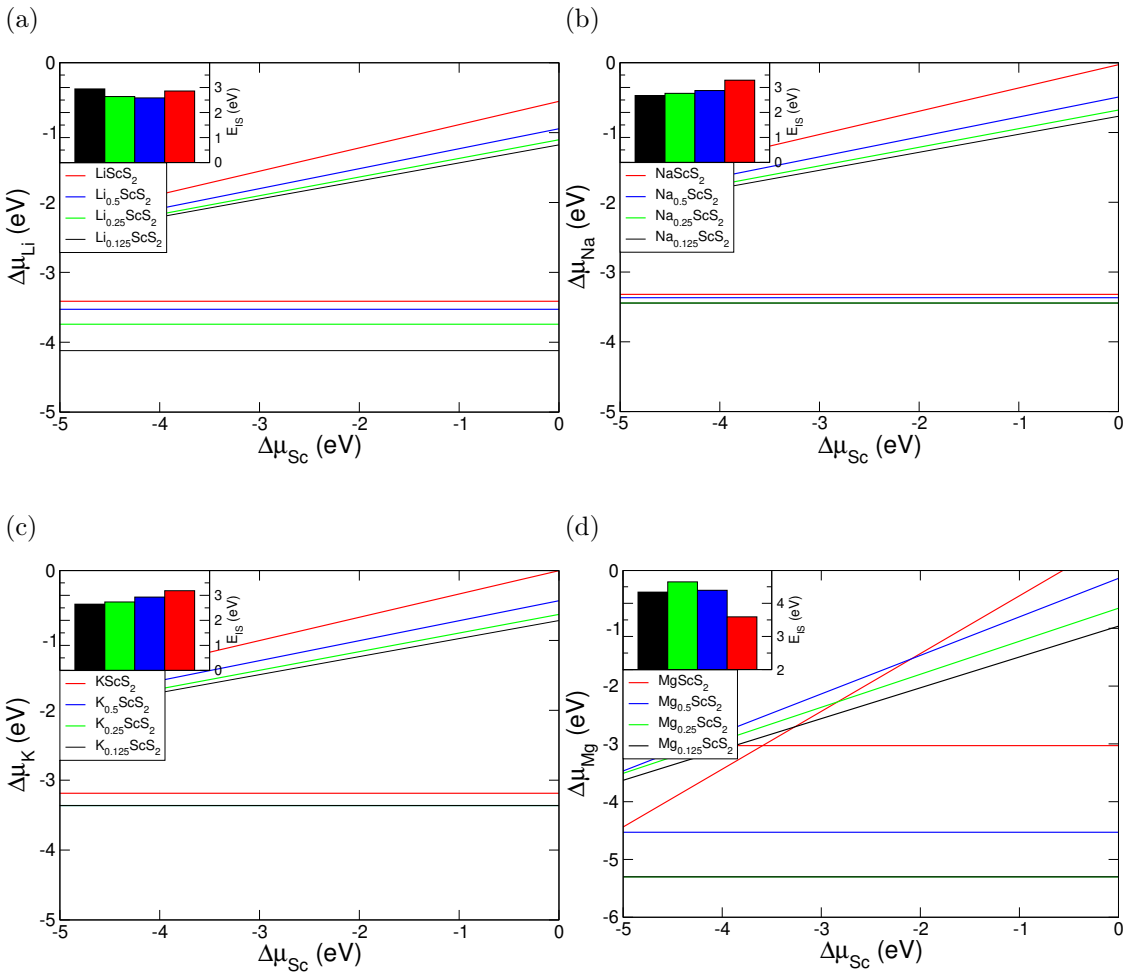

Figure S 7: S7a, S7b, S7c, and S7d show the phase diagrams for Hc-ScS_2 intercalated with different concentrations of Li, Na, K and Mg, respectively. The insets show the corresponding values of E_{IS}.

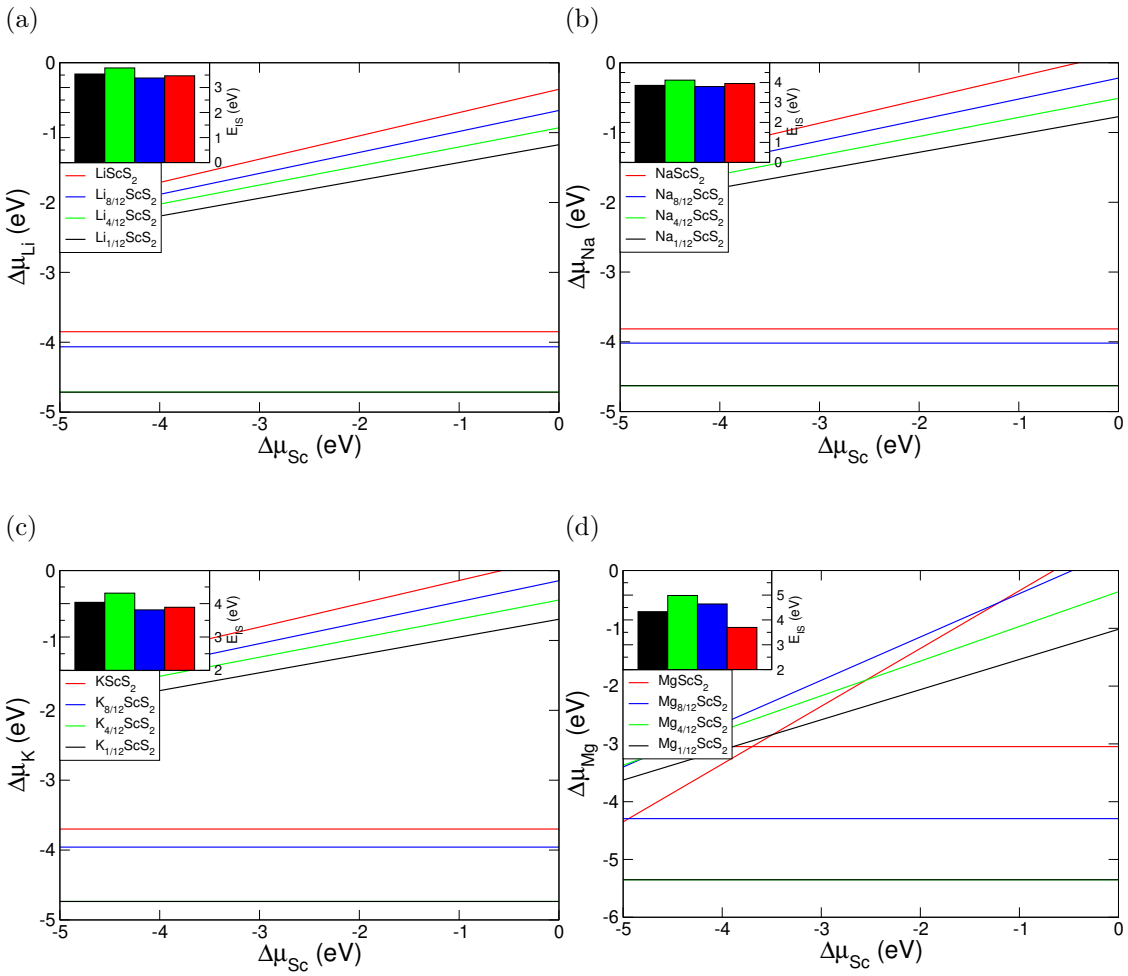

Figure S 8: S8a, S8b, S8c, and S8d show the phase diagrams for α-ScS_2 intercalated with different concentrations of Li, Na, K and Mg, respectively. The insets show the corresponding values of E_{IS}.

Phase	Intercalant	a in M_aScS_2	Old E_{IS} (eV)	Intercept (eV)	New E_{IS} (eV)
α	Na	$\frac{12}{12}$	3.949	0.134	3.815
α	K	$\frac{12}{12}$	3.891	0.192	3.699
α	Mg	$\frac{12}{12}$	3.698	0.651	3.047
α	Mg	$\frac{8}{12}$	4.644	0.350	4.293
T	Na	$\frac{8}{8}$	3.637	0.082	3.554
T	K	$\frac{8}{8}$	3.629	0.133	3.496
T	Mg	$\frac{8}{8}$	3.690	0.659	3.031
T	Mg	$\frac{4}{8}$	5.415	0.168	5.247
Hc	Na	$\frac{8}{8}$	3.592	0.562	3.030

Table S IX: Adjusted values of E_{IS} taking into account the boundary described by equation 4 in the main article. New value of E_{IS} obtained from $E_{IS}^{New} = E_{IS}^{Old} - \text{Intercept}$.

IV. RAFFLE

The pseudoRandom Approach For Finding Local Energetic minima (RAFFLE) has been developed in a similar manner to the approaches postulated by AIRSS[14], CALYPSO[15,16], CrySPY[17], and GASP[18] in the field of structure search. RAFFLE draws from said previous methodologies by successively sampling the structure space in question repeatedly in order to approach a heuristic convergence to the energy landscape of prospective new structures.

The beginning of any RAFFLE exploration consists of determining the stoichiometries of interest; taking ScS_2 with intercalant lithium as an example, the ratios of interest are 1:2:(0-1), with non integer lithium fractions corresponding to larger supercells. This suite of stoichiometries provides a set of bases for structural generation; in this case, the fully intercalated picture (e.g. Sc:S:Li 1:2:1) is considered, as the most likely to present departure from the layered phases expected in the non-intercalated system.

The process behind structure search is to generate random structures, and then rank them using a suitable metric. In the case of RAFFLE we use formation energy per atom. The process for generating the random structures is as follows. Our first stage begins with a volume estimation, which is estimated from a packing fraction approach. This range is adjusted by $\pm 50\%$ to allow for different packing radii in compounds as opposed to elemental bulk. Further details can be found in an upcoming publication devoted to discussing the full RAFFLE methodology. The unit cells are then randomly constructed. The ratios between the six unit cell defining parameters (a, b, c, α, β, γ) are determined randomly, with a skewed normal distribution designed to prevent extremely small angles and lattice constants (below the atomic radii).

Atoms are placed within the resultant unit cell according to a set of 2-, 3- and 4-body distribution functions. These functions are initially populated with structural information from databases such as the Materials Project[19], but as the data set grows to encompass relaxed structures, these structures are encoded into the distribution functions according to their relative energetic favorability; those which are more stable contribute their distributions more heavily to future generations. The full breakdown of these functions and their generation can be seen in the future publication. The essence of the methodology is distilled as follows: replicating the pseudo-local favourable chemistry of atoms leads to more energetically stable structures, thus a set of descriptors of local chemistry must be obtained

that is sufficient to replicate key features inversely. The expansion to i^{th}-body could be continued arbitrarily far, but from an anecdotal standpoint 3-body (angular) is simply not sufficient and 5-body would be exponentially more expensive than is practical, thus 4-body is a determined to be a suitable compromise. Utilising algorithms designed to place atoms in sensible locations, all the atoms are placed sequentially within the cell, according to the positions which maximise similarity between the seeded distribution functions and that of the new structure.

Once the structure is generated, the unit cell is relaxed using standard methodologies. In this case, geometric optimisation is performed using a choice of gradient descent algorithm according to energies provided by *ab-initio* methods (in this case, density functional theory). Relaxed structures are characterised and their distributions added to the aforementioned functions. This process is repeated until the apparent ground state structure has been repeated several times, and the lowest ranked structures are then considered to be the found structures. In this manuscript, our approach was limited to small unit cells of up to 16 atoms. As with all random searching methods, no search is guaranteed to find the lowest energy structure. Finding the same apparent ground state repeated multiple times is a substantial indicator that the ground state has indeed been identified.

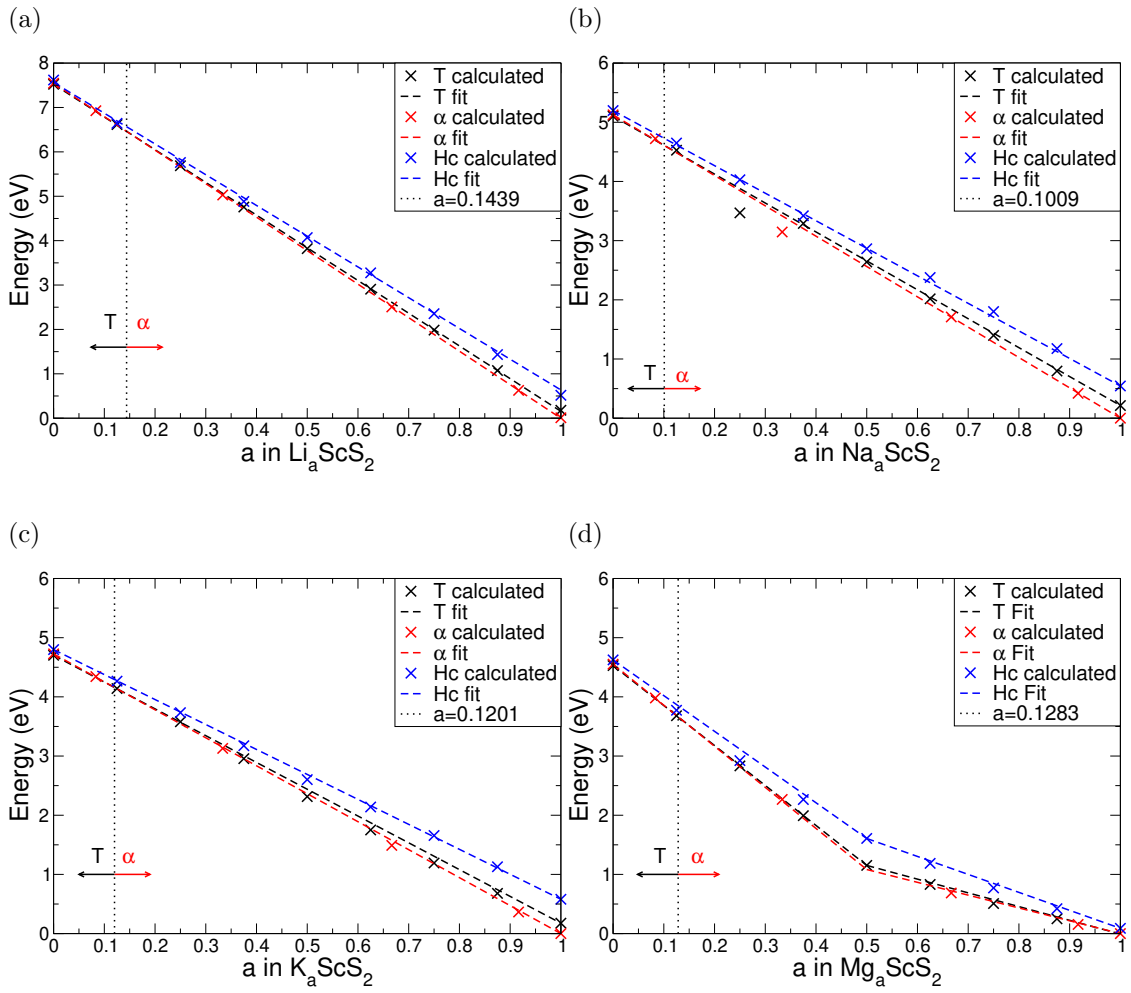

Figure S 9: Energy per formula unit of T, α and Hc phases of M_aScS_2 (M=Li,Na,K,Mg) for a range of concentrations a. S9a shows the data for Li intercalate ScS_2, S9b shows the data for Na intercalate ScS_2, S9c shows the data for K intercalate ScS_2, and S9d shows the data for Mg intercalate ScS_2. Linear fits have been presented in each to identify the crossing points.

V. BEYOND-LI PHASE CROSSOVER

To compare the relative energies of the different phases of ScS_2 intercalated with the different intercalants, and hence determine the polymorph that is energetically preferred, we present in Figure S9 energy per formula unit for each of the considered phases. For visual aid we have included a linear fits to the Li, Na, and K intercalated systems. For each of these, we can determine that the T-phase is the lowest in energy for low intercalant

concentrations (a < 0.15 in M_aScS_2, M = Li, Na, K), whereas for higher concentrations the α-phase is preferred. These boundaries are indicated in each of the Figures S9a for Li, S9b for Na, and S9c for K with the vertical dashed lines. However, for magnesium the double valency results in two changes to the oxidation state of the host material. This can be seen with the change in gradient of the line from $0 <$ a < 0.5 and $0.5 <$ a < 1. It it noted that for all of the phases and each of the intercalants, the Hc-phase of ScS_2 is always the highest in energy, hence we focused on the T- and α-phases in the main article.

VI. PHONONS

A. Phonon Band Structures

In the main article we have used the thermodynamic phase diagrams to determine stability of the intercalated materials against conversion, but it is also important to assess whether these materials are dynamically stable by considering their phonon modes. Figures S10, S11, and S12 present the phonon band structure for the T-ScS_2, Hc-ScS_2, and α-ScS_2 and their intercalated forms respectively, with the exception of the Hc-ScS_2 phase. This phase is both energetically unfavourable and the calculations of phonon displacements did not electronically converge within DFT. Thus we have not calculated the phonon band structure for this phase, as we believe its relevance is very low. For each of the bulk phases, it is clear to see the presence of imaginary phonon modes which result in dynamic instability. However, upon intercalation to $MScS_2$, these imaginary phonon modes are removed due to the addition of the intercalant, showing the intercalated structure to be dynamically stable.

By comparing the phonon band structures for the different intercalants, similar features can be seen for the Group I metals. The key difference between them being a reduction in frequency of the optical bands. This is highlighted at the zone centre, with the highest optical band having frequency of 12.19 THz (406.49 cm^{-1}) for lithium intercalation, 11.52 THz (384.12 cm^{-1}) for sodium interalation, and 11.10 THz (370.21 cm^{-1}) for potassium intercalation. This reduction of $\sim$0.5 THz between each. There is a significant change in the phonon band structure for magnesium intercalation, however, with the resulting phonon bands being much less dispersive than those of the Group I intercalants.

Evaluation of the phonon band structures for intermediate lithium concentrations allows us to determine the lowest concentration of lithium we can access before the intercalated layered structure becomes dynamically unstable. For the α-phase, the instability seen in $Li_{\frac{1}{12}}ScS_2$ and $Li_{\frac{2}{12}}ScS_2$ structure. Similarly for T-ScS_2, $Li_{\frac{1}{8}}ScS_2$ is unstable whereas $Li_{\frac{2}{8}}ScS_2$ is not. We can therefore conclude that the lowest concentration of lithium that can be reached (corresponding to the depth of discharge and hence the maximum reversible capacity) in ScS_2 lies somewhere below a = 0.25.

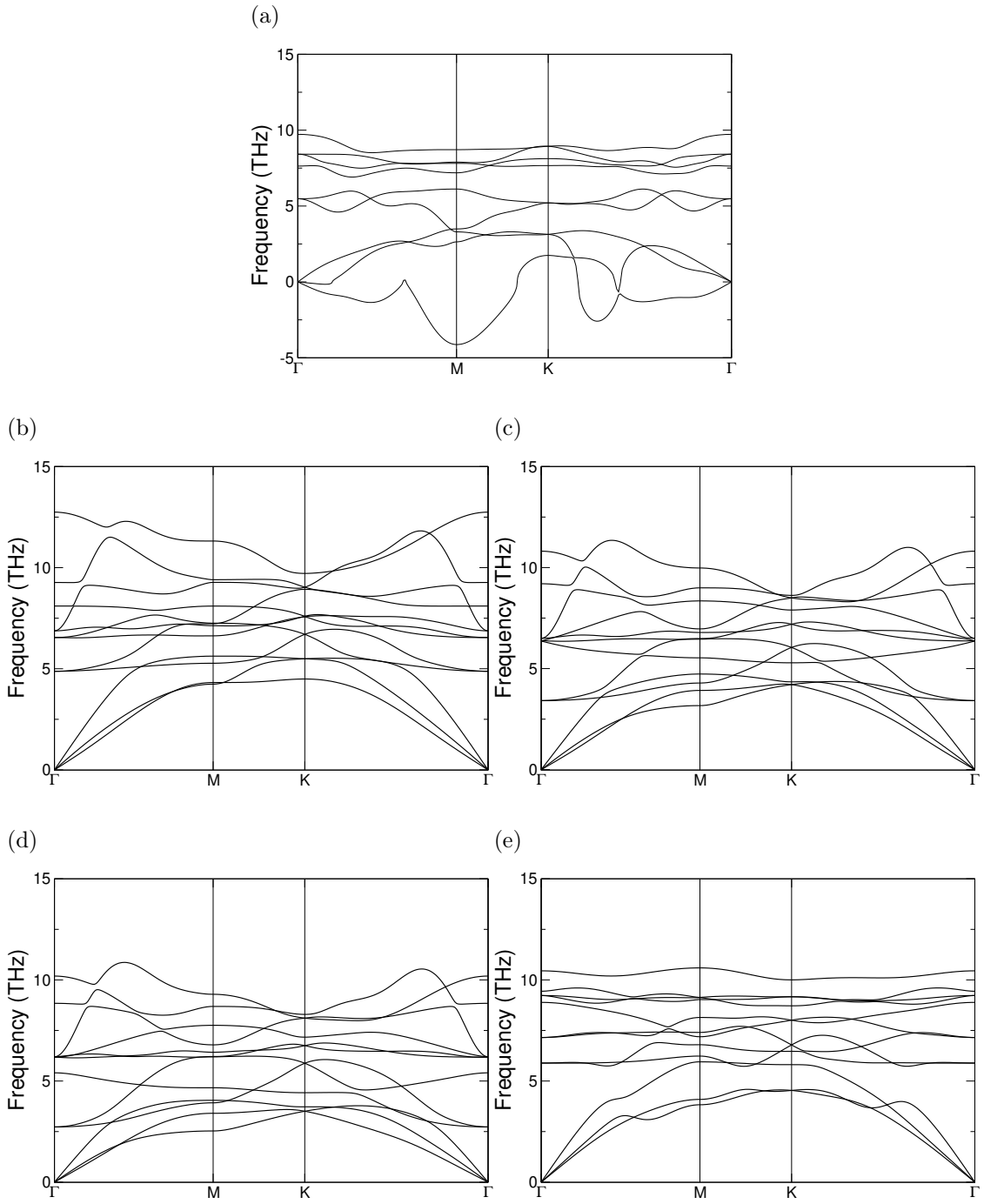

Figure S 10: Phonon band structures for T-ScS_2 and T-ScS_2 intercalated with different metal species. S10b shows the band structure for $LiScS_2$, S10c shows the band structure for $NaScS_2$, S10d shows the band structure for $KScS_2$, and S10e shows the band structure for $MgScS_2$.

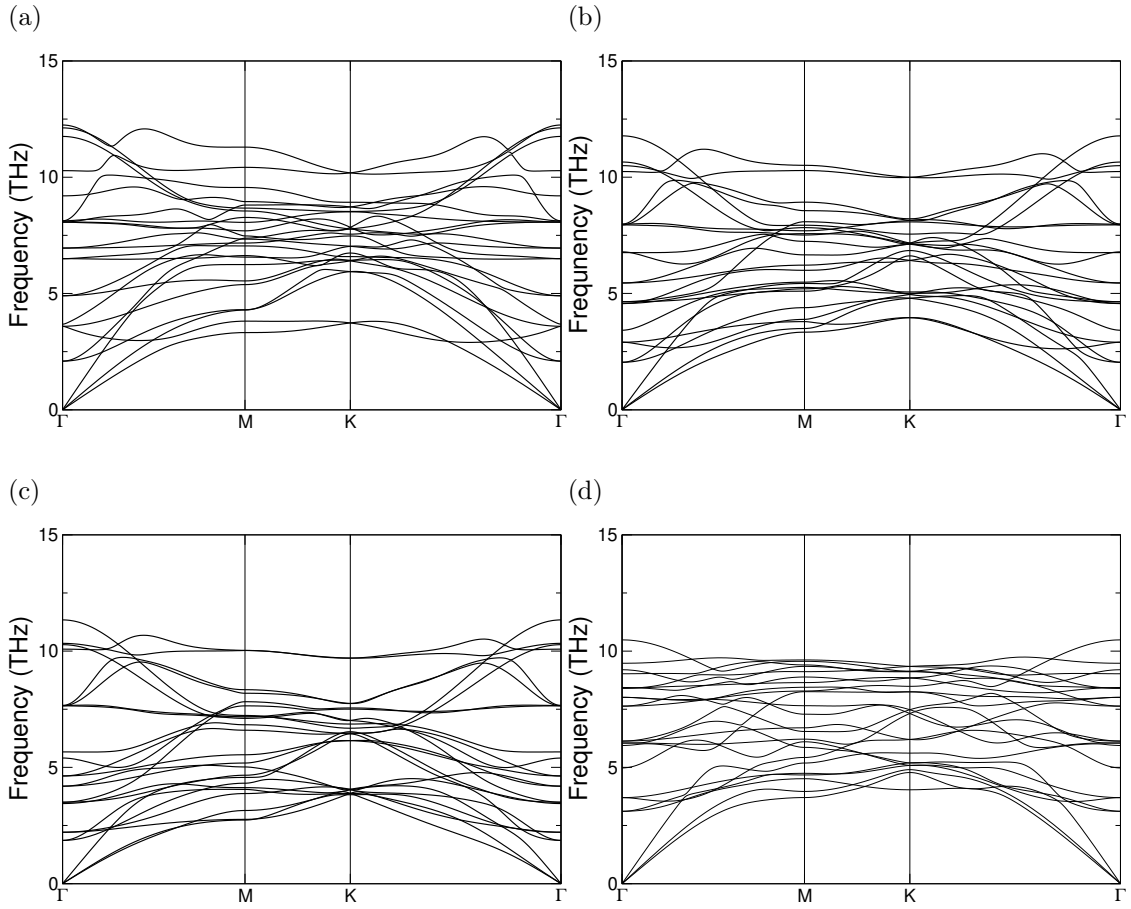

Figure S 11: Phonon band structures for Hc-ScS_2 and Hc-ScS_2 intercalated with different metal species. S11a shows the band structure for $LiScS_2$, S11b shows the band structure for $NaScS_2$, S11c shows the band structure for $KScS_2$, and S11d shows the band structure for $MgScS_2$.

B. Dynamic Corrections

In most scenarios, the total internal energy obtained from DFT calculations is useful for comparisons for different phases of the same material, but it is not able to account for dynamic effects such as zero-point energy (ZPE) motion and vibrations due to finite temperature. To include these dynamic effects we instead use,

$$U^{Dyanmic} = U^{DFT} + U^{ZPE} + TS^{vib}, \tag{S24}$$

where U^{DFT} is the energy obtained from the DFT calculation (presented in Figure S9),

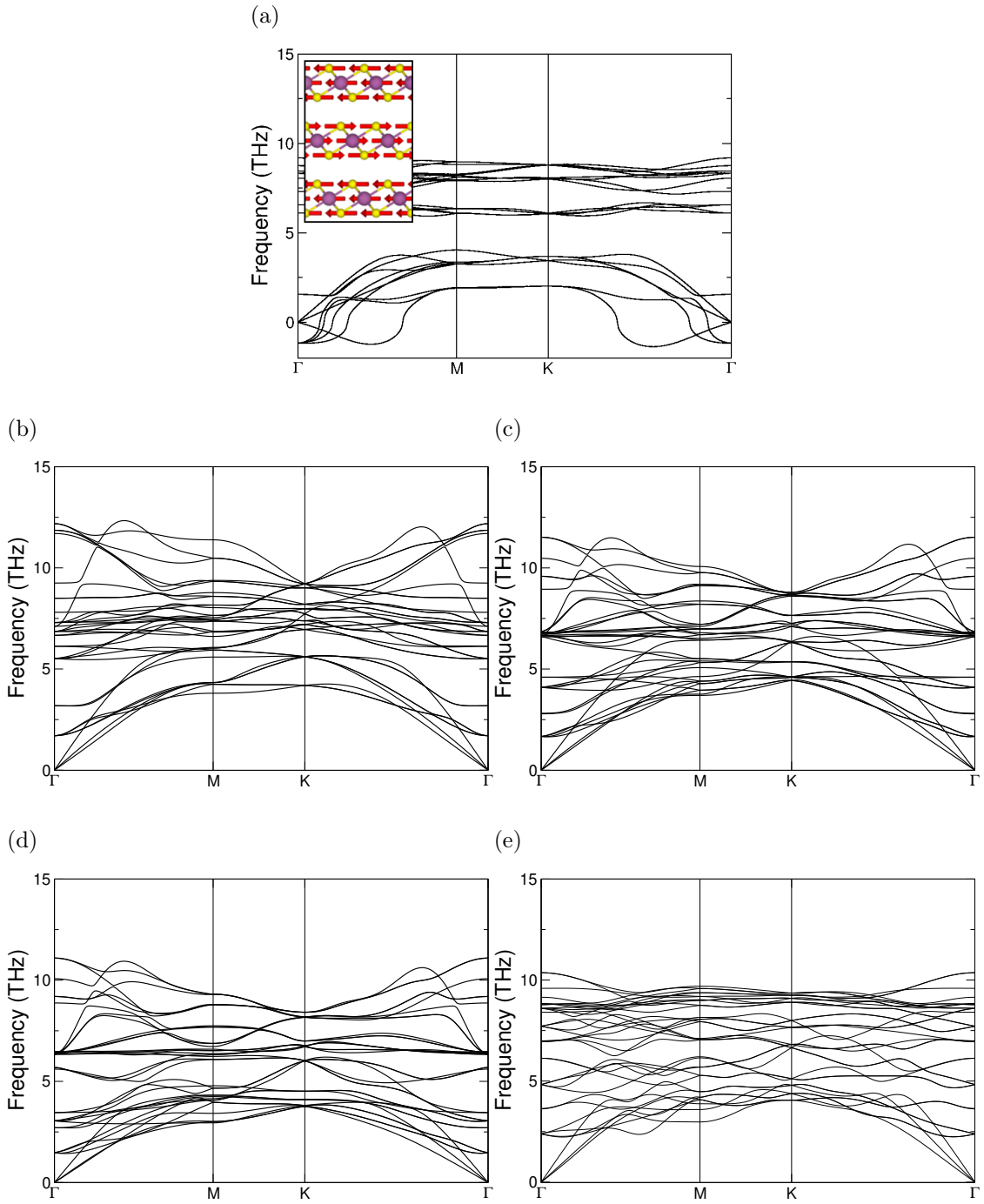

Figure S 12: Phonon band structures for pristine α-ScS_2, and α-ScS_2 intercalated with different metal species. S12a shows the phonon band structure for pristine bulk α-ScS_2. Similarly, the band structures for $LiScS_2$, $NaScS_2$, $KScS_2$, and $MgScS_2$ are shown in S12b, S12c, S12d, and S12e respectively.

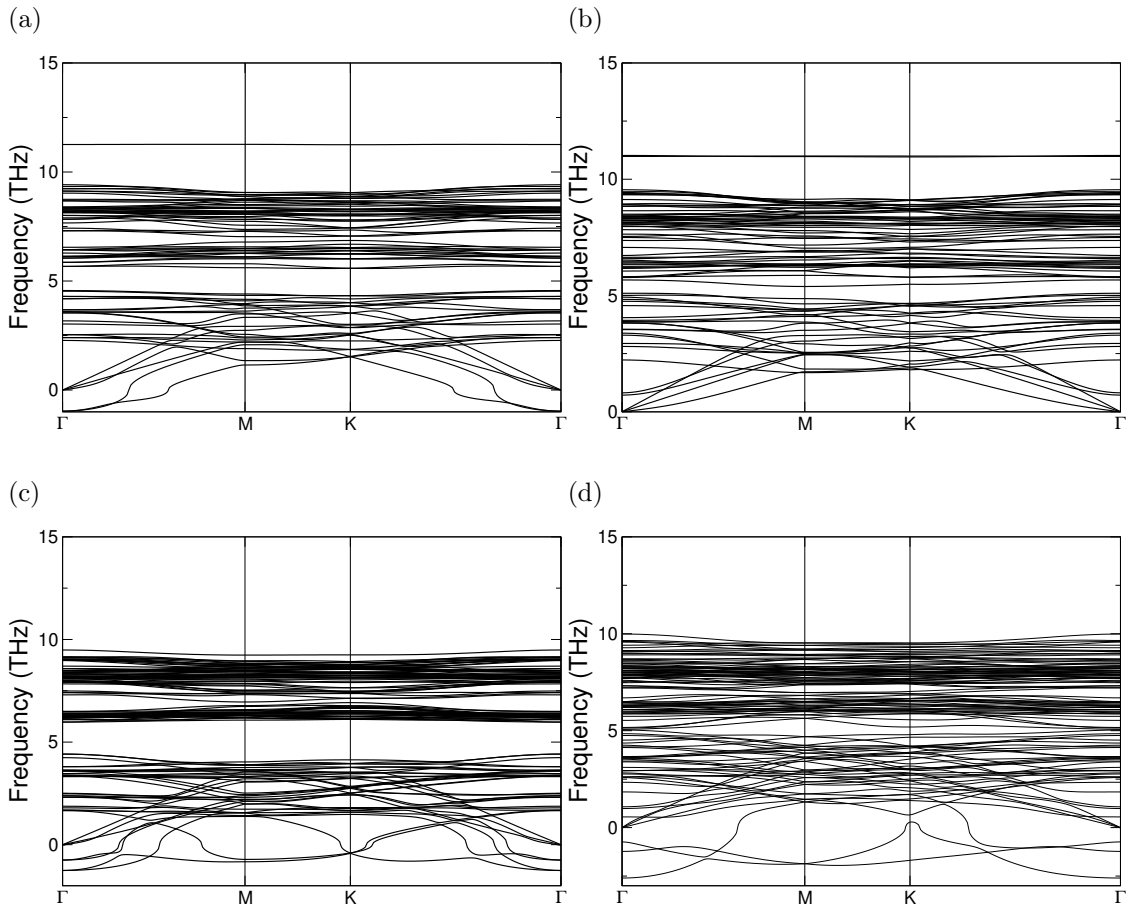

Figure S 13: Phonon band structures for T-ScS_2 intercalated to $Li_{\frac{1}{8}}ScS_2$ (S13a) and $Li_{\frac{2}{8}}ScS_2$ (S13b), and for α-ScS_2 intercalated to $Li_{\frac{1}{12}}ScS_2$ (S13c), and $Li_{\frac{2}{12}}ScS_2$ (S13d).

U^{ZPE} is the energy associated with the zero-point motion of the lattice, and TS^{vib} is the energy from finite temperature vibrations. The last two of these terms are given by,

$$U^{ZPE} = \sum_{\nu,\mathbf{q}} \frac{1}{2}\hbar\omega_{\nu,\mathbf{q}}, \tag{S25}$$

and,

$$S^{vib} = \frac{1}{2T}\left[\sum_{\nu,\mathbf{q}} \hbar\omega_{\nu,\mathbf{q}} \coth\left(\frac{\hbar\omega_{\nu,\mathbf{q}}}{2k_BT}\right)\right] - k_B\left[\sum_{\nu,\mathbf{q}} \ln\left(2\sinh\left(\frac{\hbar\omega_{\nu,\mathbf{q}}}{2k_BT}\right)\right)\right]. \tag{S26}$$

The size of the TS^{vib} corrections are presented in Figure S14 for each of the phases intercalated with each of the intercalants, and the values of U^{ZPE}, $TS^{vib}(T = 400\text{ K})$, and the

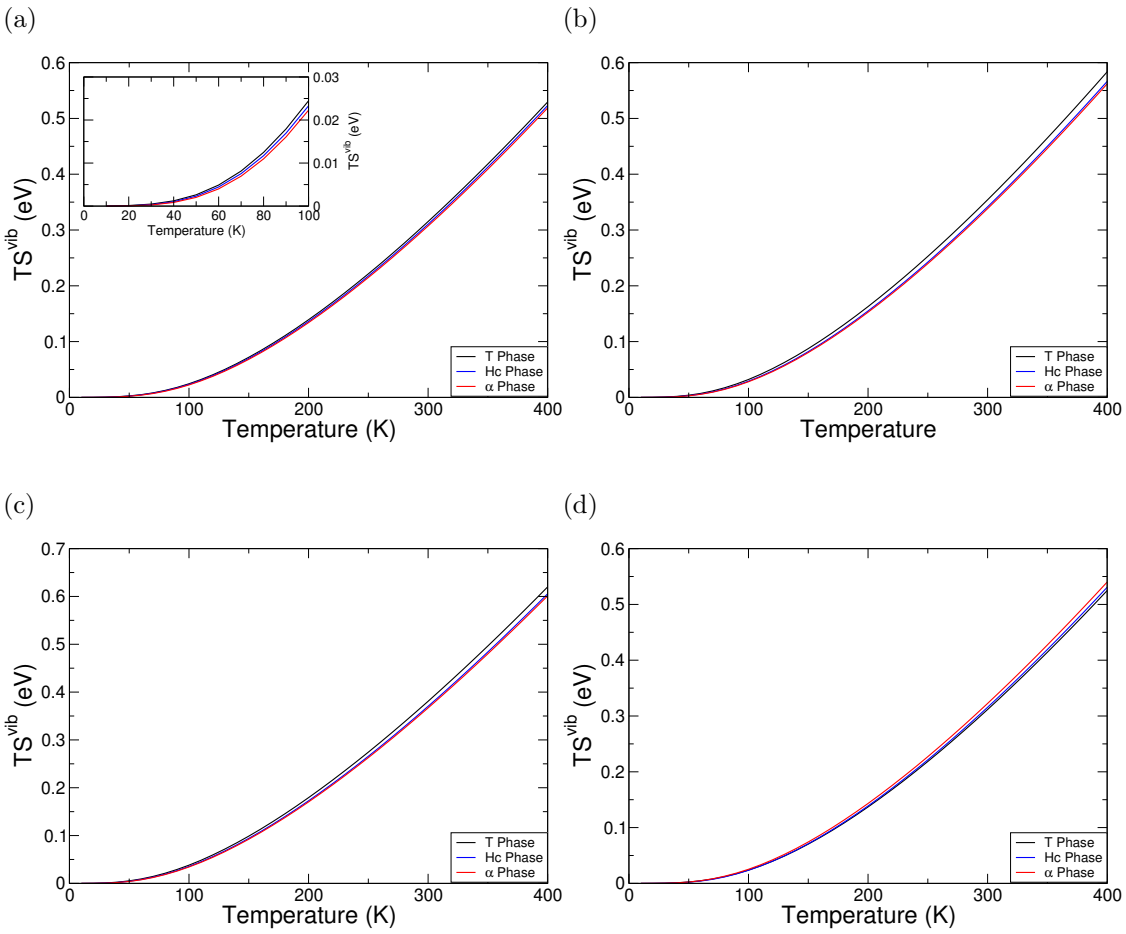

Figure S 14: Corrections to the total energy that would arise from finite-temperature lattice vibrations in intercalated ScS_2. The figures presented are for $LiScS_2$ (S14a), $NaScS_2$ (S14b), $KScS_2$ (S14c), and $MgScS_2$ (S14d).

resultant correction ($U^{ZPE} + TS^{vib}(T = 400\text{ K})$) are presented in Table SX. The values of $\omega_{\nu,\mathbf{q}}$ were obtained from the phonon band structures presented above.

For each of the Group I intercalants, the T-phase has the largest TS^{vib} value whilst the α-phase has the smallest. The ordering is reversed for magnesium intercalation. Interestingly, the corrections that arise from considering these dynamic effects for each phase are all of the order of 0.7 eV, with minor variation (< 0.02 eV) for each of the intercalants. As a result, the ordering of the intercalated phases presented in Figure S9 is not affected by the inclusion of these additional terms, and so these corrections have not been included in the results presented in the main article.

Intercalant	Phase	U^{ZPE} (eV)	$TS^{vib}(T = 400$ K) (eV)	Correction (eV)
Li	T	0.174	0.529	0.704
Li	Hc	0.176	0.523	0.699
Li	α	0.176	0.519	0.695
Na	T	0.154	0.584	0.737
Na	Hc	0.158	0.566	0.725
Na	α	0.159	0.562	0.721
K	T	0.142	0.620	0.762
K	Hc	0.146	0.606	0.752
K	α	0.146	0.601	0.747
Mg	T	0.175	0.525	0.700
Mg	Hc	0.170	0.531	0.701
Mg	α	0.168	0.540	0.708

Table S X: Dynamics corrections to the total energy of intercalated ScS_2. U^{ZPE} is the zero-point energy calculated using equation (S25), and $TS^{vib}(T = 400$ K) is the energy arising from finite-temperature vibrations calculated using equation (S26) at a temperature of $T = 400$ K.

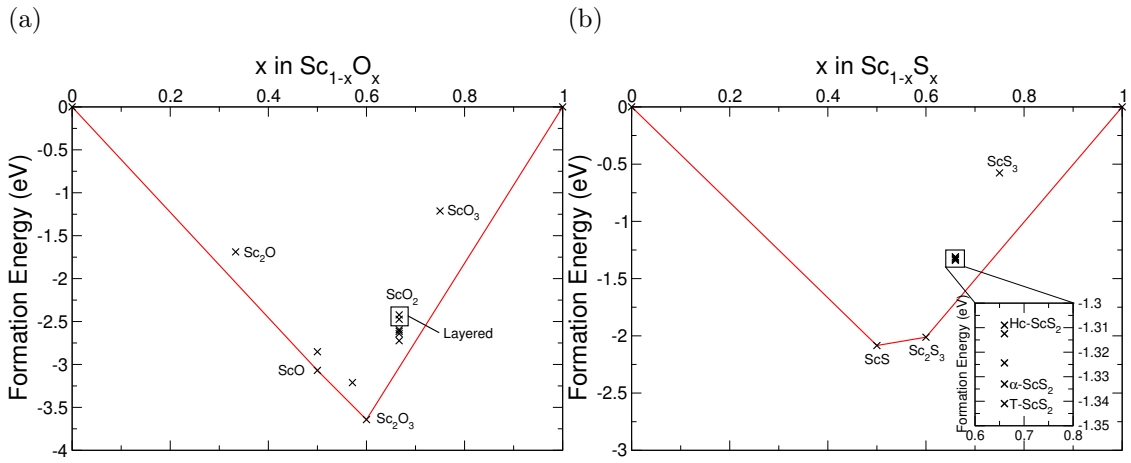

Figure S 15: Convex hulls for Sc-O (S15a) and Sc-S (S15b) compounds.

VII. CONVEX HULL FOR SC-O AND SC-S COMPOUNDS

To investigate other possible structures/compounds that could form upon synthesis of ScS_2, we have constructed a convex hull. However, as there are a limited number of scandium sulfide compounds that have been presented in the literature and on databases such as the ICSD and Materials Project[19], we have also considered scandium oxide compounds to inform us of potential scandium sulfide analogues.

Figure S15a presents the generated convex hull for compounds of scandium and oxygen with different stoichiometries. We note that the compounds with stoichiometry ScO_2 do not lie on the hull. Furthermore, the layered structures are the least energetically favourable of the structures considered for that composition, lying 0.62 eV above the hull. Of the structures investigated for the ScO_2 composition, the lowest energy belongs to the monoclinic structure similar to that of Baddeleyite. Clearly, the layered ScO_2 structure would be prone to form the monoclinic structure instead, or a decomposition reaction $2ScO_2 \rightarrow Sc_2O_3 + \frac{1}{2}O_2$

We find similar results for the scandium sulfide compounds, with the various ScS_2 structures lying above the hull. However, we find for the sulfides that the layered structures are the most favourable, and lie closer to the hull, with T-ScS_2 being $\sim$0.37 eV above the hull.

Phase	Intercalant Species	Charge of Sc (|e|)	Charge of S (|e|)	Charge of Intercalant (|e|)
T	-	2.21	-1.11	-
	Li	2.23	-1.55	0.88
	Na	2.23	-1.54	0.85
	K	2.23	-1.51	0.79
	Mg	2.01	-1.84	1.67
Hc	-	2.19	-1.10	-
	Li	2.21	-1.55	0.88
	Na	2.22	-1.53	0.85
	K	2.20	-1.50	0.78
	Mg	1.95	-1.82	1.69
α	-	2.21	-1.11	-
	Li	2.23	-1.56	0.88
	Na	2.23	-1.54	0.85
	K	2.23	-1.51	0.80
	Mg	2.02	-1.85	1.69

Table S XI: Bader charge values of species in pristine and fully-intercalated ScS_2, for the different phases considered in this work.

VIII. CHARGE ANALYSIS

It is useful to discuss the charge transfer upon intercalation, as charge transfer is ultimately the source of the energy storage in electrodes. We first do this with Bader charge analysis, the data for which is presented in Table SXI. We first note that the intercalant charge remains unchanged with intercalation into the different phases of ScS_2, highlighted best with lithium which possesses a charge of 0.88 |e| in each of the phases.

Between the different intercalants, though, there is a more significant difference. In α-ScS_2, the charge on lithium is 0.88 |e|, the charge on sodium is 0.85 |e|, and the charge on potassium is 0.80 |e|. Magnesium, being a Group II element, possesses twice the valence electrons as its Group I neighbour of sodium. It is therefore unsurprising to see that magnesium possesses a charge of 1.69 |e|, twice the charge of sodium.

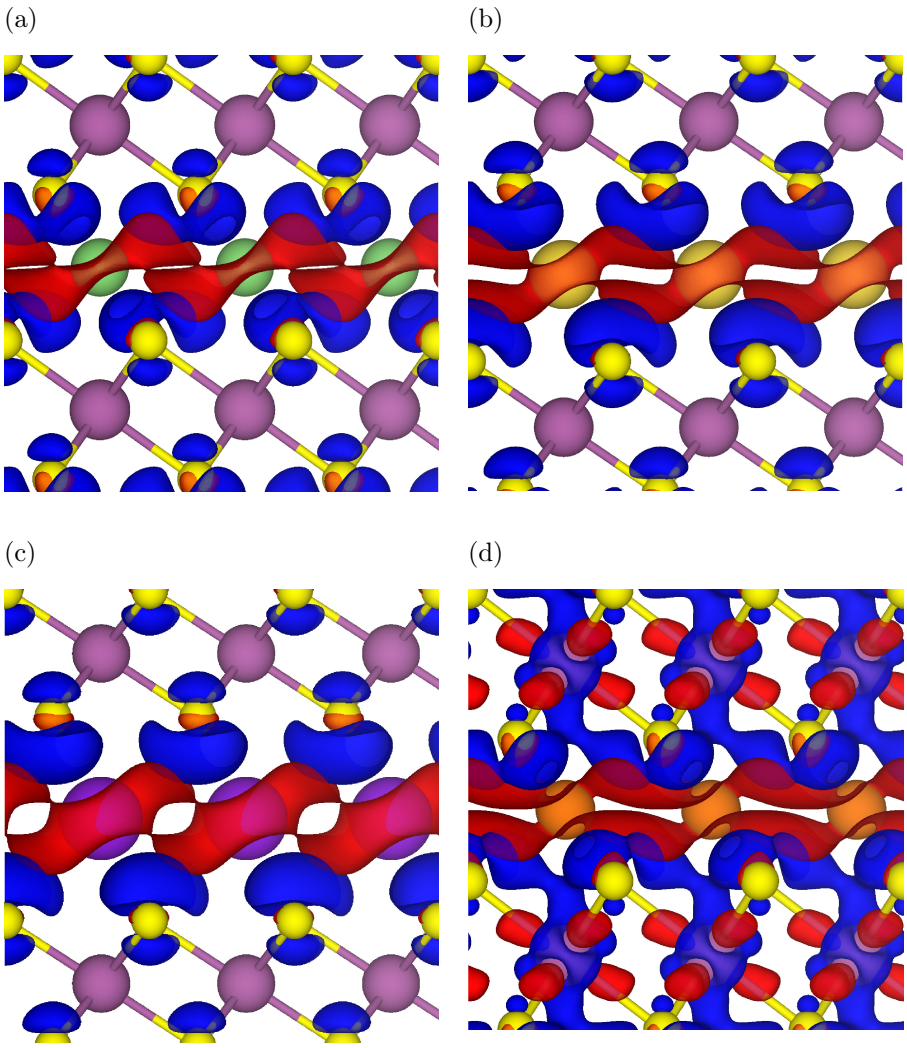

Figure S 16: The charge difference plots arising from intercalation of T-ScS_2 obtained using $\Delta\rho = \rho_{MScS_2} - [\rho_M + \rho_{ScS_2}]$ for intercalants M = Li (S16a), Na (S16b), K (S16c) and Mg (S16d). In these, red isosurfaces show electron depletion and blue isosurfaces show electron accumulation. The ScS_2 layers are shown with purple and yellow atoms.

To evaluate charge transfer between intercalant ions and the host ScS_2 more rigorously, the geometrically-relaxed intercalated structures were separated into the host ScS_2 and the intercalant ions. Keeping the positions of the ions the same as in the intercalated material, the electronic charge densities were obtained. By comparing the charge density of the full structure with those of the ScS_2 structure and the intercalant[20], i.e. $\Delta\rho = \rho_{MScS_2} - [\rho_M + \rho_{ScS_2}]$, it is possible to comment on the charge transfer upon intercalation. This is shown in Figure S16 for the T-phase of ScS_2 intercalated with each of lithium, sodium, potassium,

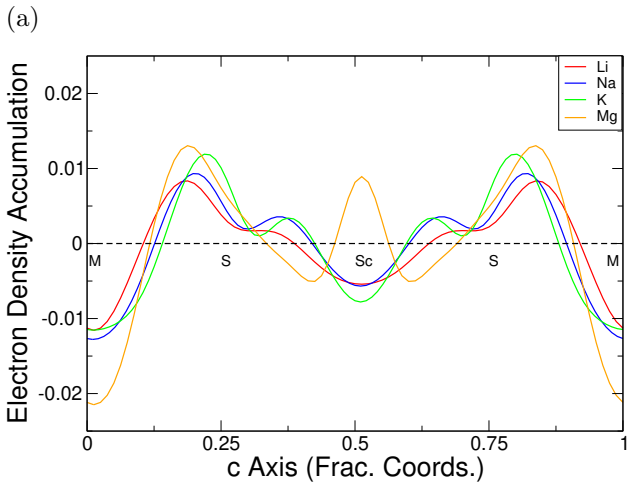

Figure S 17: The planar-average of $\Delta\rho = \rho_{\mathrm{MScS_2}} - [\rho_{\mathrm{M}} + \rho_{\mathrm{ScS_2}}]$ for intercalants M = Li (red), Na (blue), K (green) and Mg (orange). Positive values correspond to regions of electron accumulation, and negative values correspond to regions of electron depletion. The black dashed line indicates zero change. Labels indicating the positions of the constituent atoms have also been included, where the repeated 'M' label shows the periodicity of the cell.

and magnesium, and the planar average values are presented in Figure S17.

For each of the Group I intercalants, it is clear to see in Figure S16 the loss of electronic charge from the intercalant into a bond with the sulfur atom, shown with the red (depletion) regions around the intercalant, and the blue (accumulation) regions. This is further highlighted with the planer-averaged values of Figure S17, where we notice the peaks in the electron density accumulation around c = 0.2 and c = 0.8. Interestingly, we also notice a further transfer of charge from the scandium to the sulfur-scandium bonding. For magnesium, we see a larger loss of electronic charge from the magnesium, corresponding to approximately double that of the Group I intercalants, as would be expected. This charge can again be seen to collect in the intercalant-sulfur bonding region. However, upon magnesium intercalation the scandium appears to gain electrons from the scandium-sulfur bonding region.

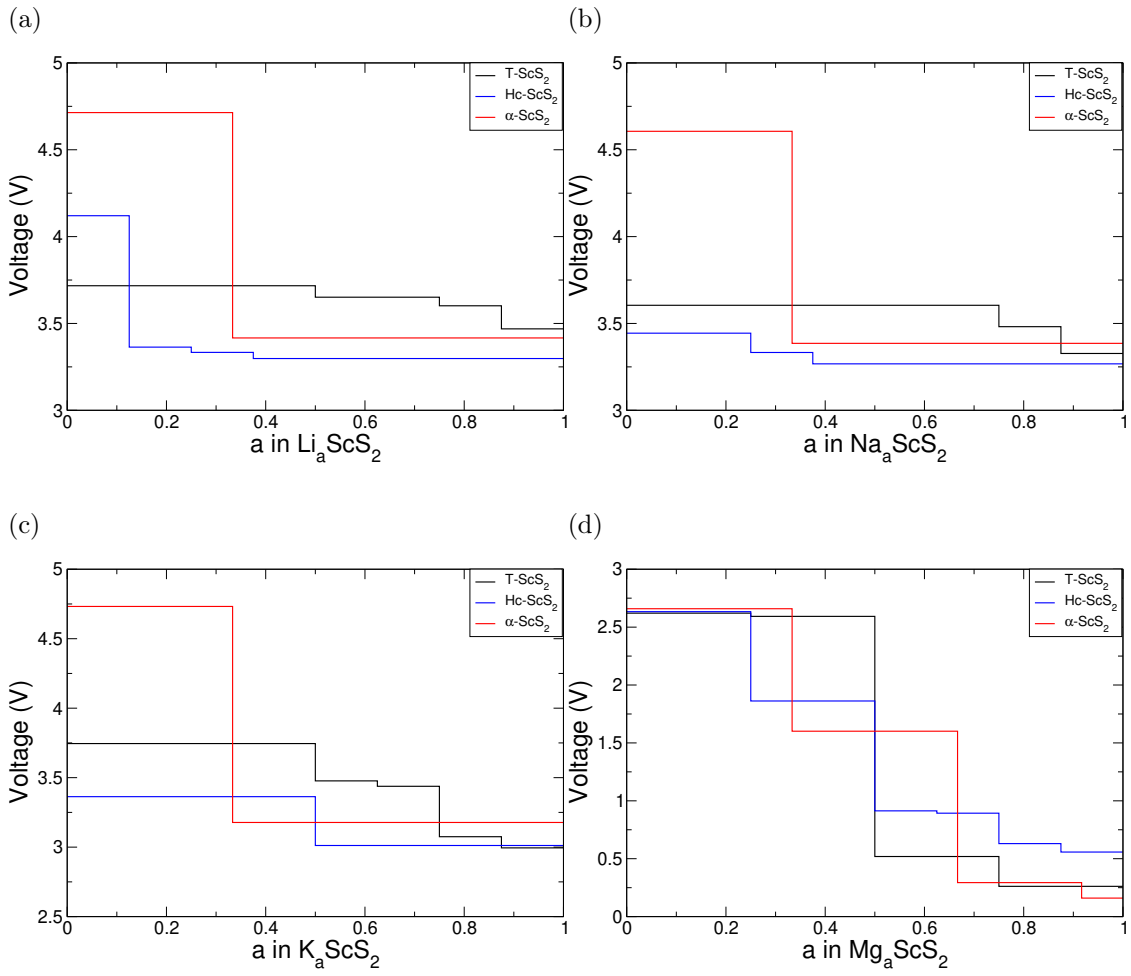

Figure S 18: Intercalation voltages obtained when ScS_2 is intercalated with lithium (S18a), sodium (S18b), potassium (S18c), and magnesium (S18d).

IX. VOLTAGES FOR OTHER SCS_2 PHASES

In the main article we focus on the α-phase of ScS_2 and here we include the obtained voltage profiles for the T- and Hc-phases intercalated with Li, Na, K and Mg. In Figure S18 we compare the voltages for each of the ScS_2 phases with each of the intercalants. With intercalation with the Group I metals, the α-phase initially demonstrates a larger voltage (of over 4.5 V) than the other phases. However, the significant drop it experiences brings the voltage in line with those of the T- and Hc-phases.

For lithium intercalation, the average intercalation potentials are 3.655 V, 3.414 V, and 3.977 V for the T-, Hc-, and α-phases, respectively. Similarly, the voltages for sodium

intercalation are 3.554 V (T), 3.320 V (Hc), and 3.874 V (α), and for potassium intercalation the voltages are 3.496 V (T), 3.187 V (Hc), and 3.799 V (α). These show that the voltages of the α-phase are greater than those for the T-phase, which are greater than the Hc-phase. For magnesium intercalation, the voltages are 1.499 V (T), 1.498 V (Hc), and 1.474 V (α), where we see the ordering is different, and the differences between each of the voltages is much lower ($\sim$0.03 V).

X. HSE RESULTS

With the use of the HSE06 hybrid functional, we note the intercalation voltage is significantly increased. We also note differences in the constructed phase diagrams, and hence the values of E_{IS}. We note that the diagonal line, corresponding to the boundary between the interclated ScS_2 and the Li_2S crystal, remains relatively unchanged. The discrepancy between the phase diagrams using the HSE06 and PBE functionals, therefore, arises from the modification to the horizontal line, corresponding to the boundary between the intercalated and pristine ScS_2 structure. Across each of the phases and intercalants presented here, the amount that the horizontal line is modified with the use of HSE06 varies, though it is consistently shifted downwards (hence increasing the region of stability). However, these results do not change the main conclusions of the article, nor invalidate the potential of ScS_2 as a cathode material.

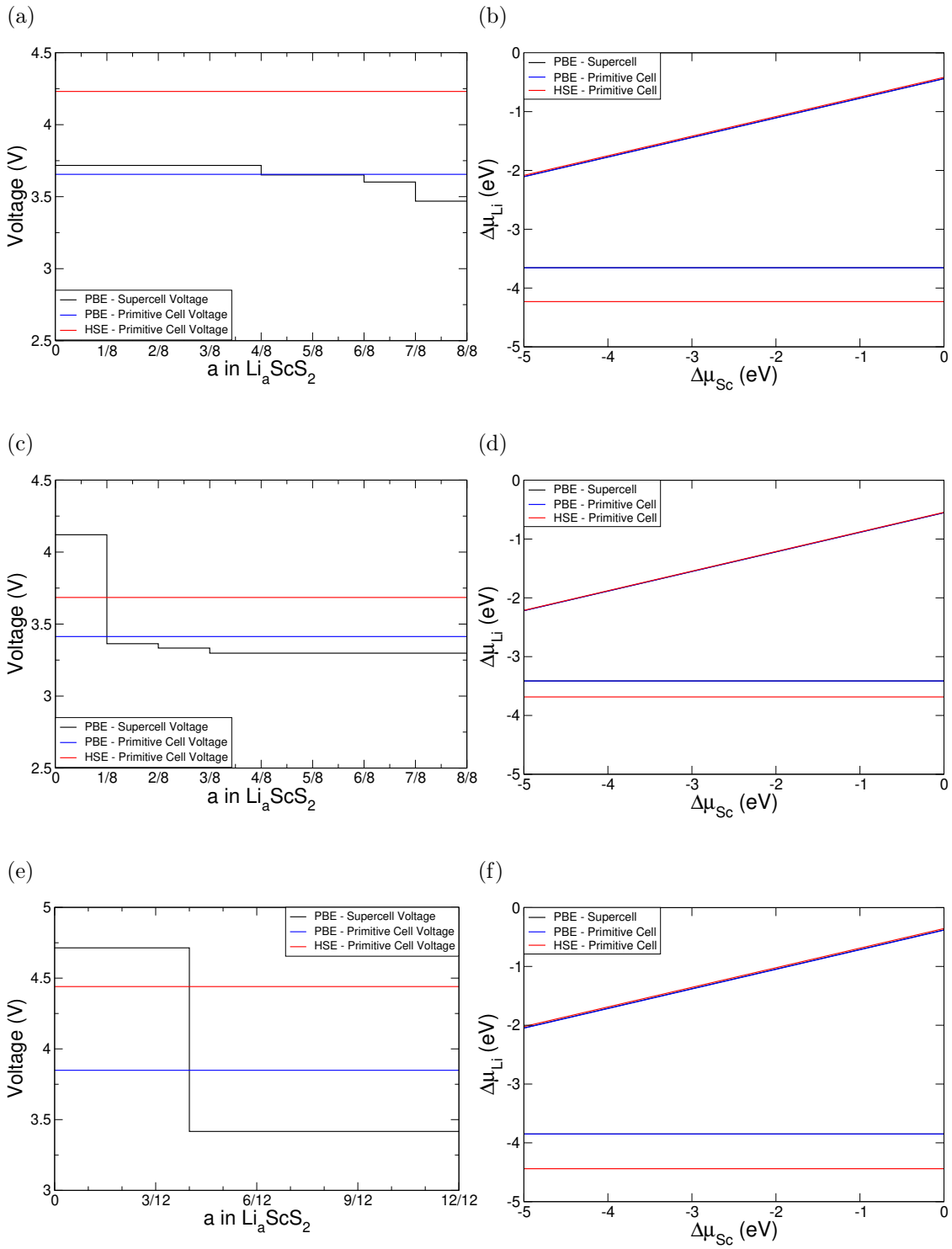

Figure S 19: Comparison of PBE and HSE06 results for the different phases of ScS_2 intercalated with Li. S19a, S19c, and S19e show the comparison of intercalation potentials for T-, Hc-, and α-phases, respectively. S19b, S19d, and S19f show the comparison of phase diagrams for T-, Hc-, and α-phases, respectively, for an intercalation concentration $LiScS_2$.

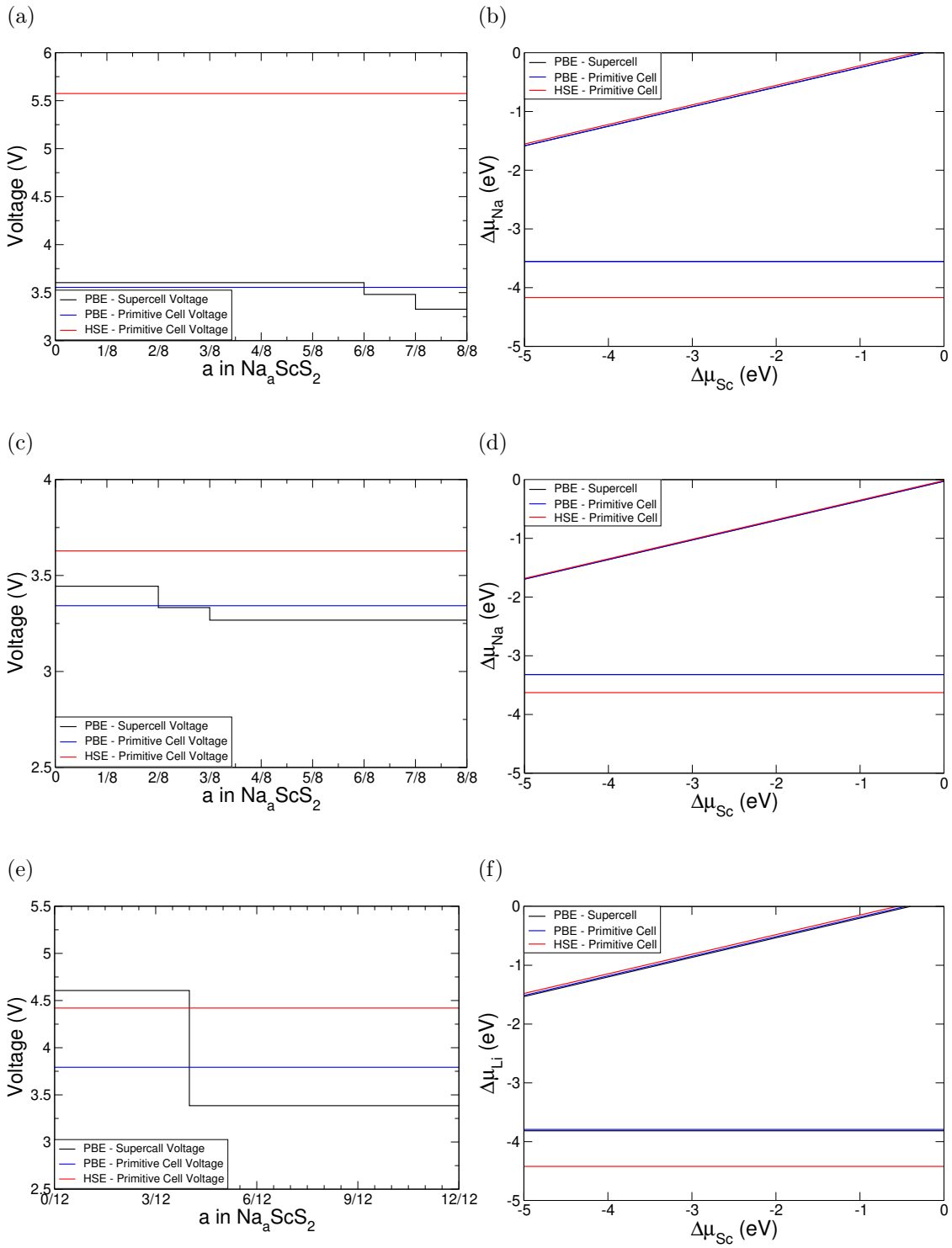

Figure S 20: Comparison of PBE and HSE06 results for the different phases of ScS_2 intercalated with Na. S20a, S20c, and S20e show the comparison of intercalation potentials for T-, Hc-, and α-phases, respectively. S20b, S20d, and S20f show the comparison of phase diagrams for T-, Hc-, and α-phases, respectively, for an intercalation concentration $NaScS_2$.

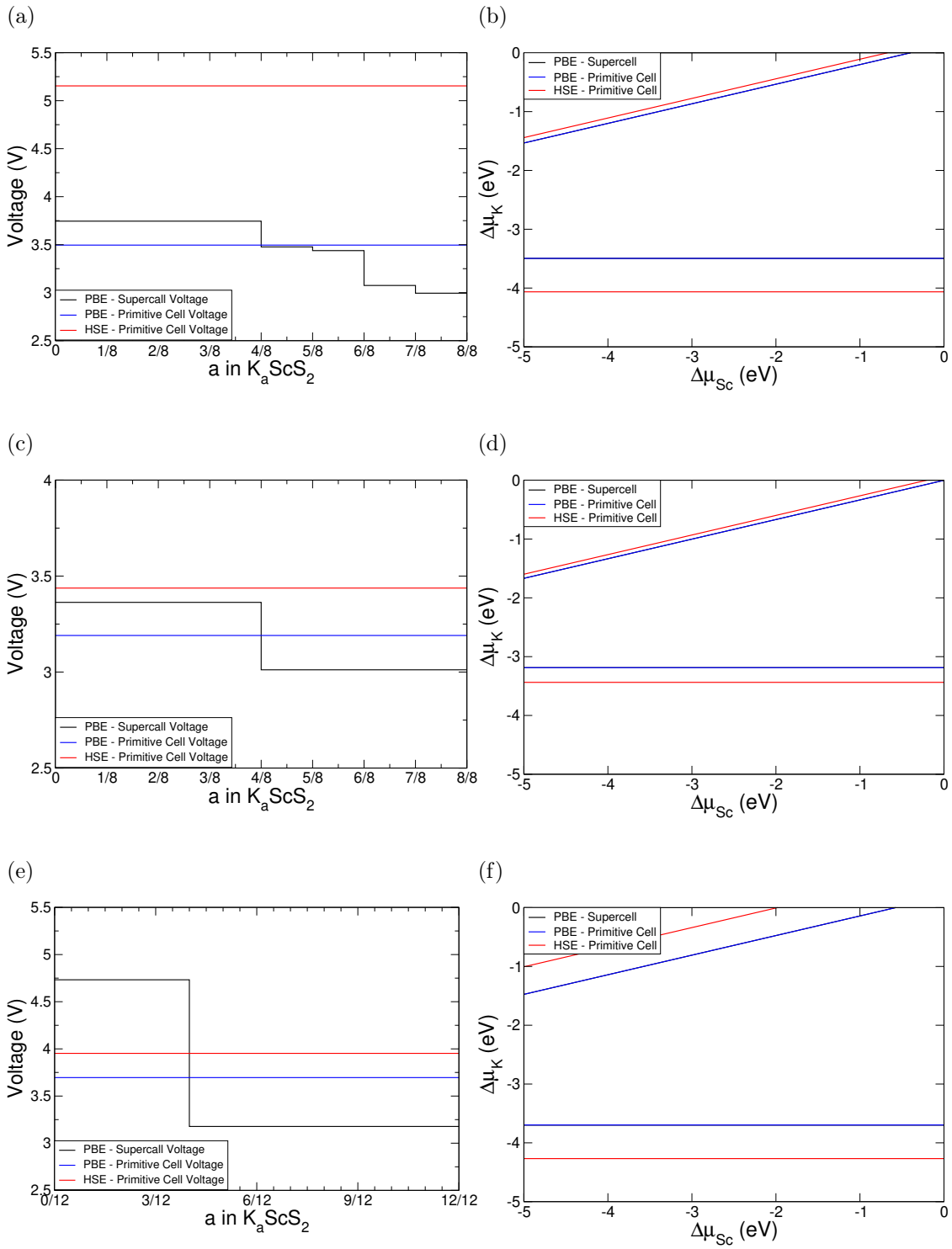

Figure S 21: Comparison of PBE and HSE06 results for the different phases of ScS_2 intercalated with K. S21a, S21c, and S21e show the comparison of intercalation potentials for T-, Hc-, and α-phases, respectively. S21b, S21d, and S21f show the comparison of phase diagrams for T-, Hc-, and α-phases, respectively, for an intercalation concentration $KScS_2$.

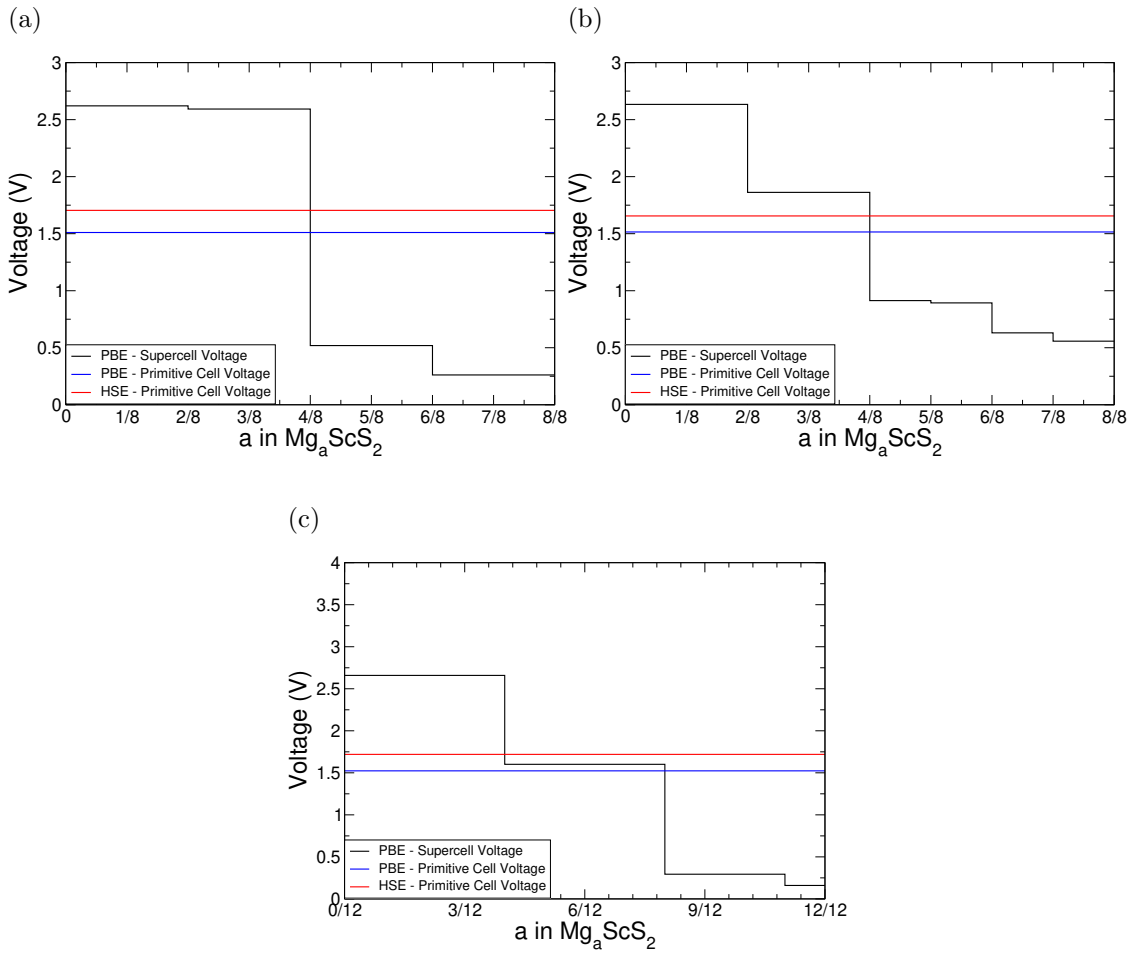

Figure S 22: Comparison of PBE and HSE06 results for the different phases of ScS_2 intercalated with Mg. S22a, S22b, and S22c show the comparison of intercalation potentials for T-, Hc-, and α-phases, respectively.

XI. ELECTRONIC STRUCTURE

We present the electronic band structure and orbital-decomposed density of states (DOS) for pristine ScS_2 (Figure S23), $LiScS_2$ (Figure S24), $NaScS_2$ (Figure S25), $KScS_2$ (Figure S26), and $MgScS_2$ (Figure S27). We see that each of the phases of pristine ScS_2 is conducting, but upon intercalation to $MScS_2$ (M = Li, Na, K), the material becomes insulating, with sizeable gaps of approximately 1.5 eV (using the PBE functional). Upon intercalation to $MgScS_2$, the material is conducting, though this is due to the double valency of magnesium compared to the Group I elements. Indeed, we see that with filling to $Mg_{0.5}ScS_2$, corresponding to the same charge transfer as with the Group I elements, the material is insulating (see Figure S28).

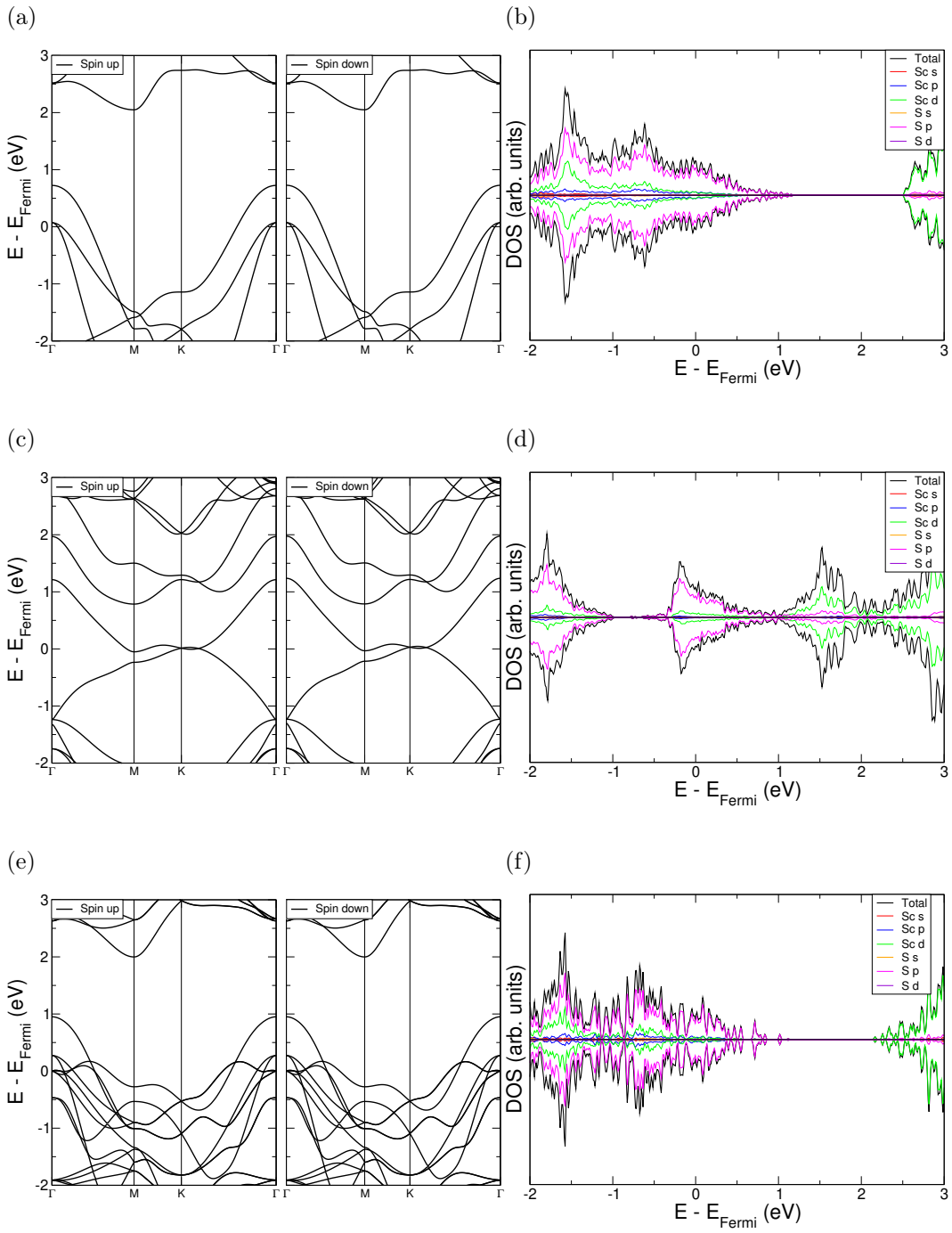

Figure S 23: Electronic band structures and orbital-decomposed density of states for pristine phases of ScS_2. S23a, S23c and S23e present the band structures along high symmetry routes for T-ScS_2, Hc-ScS_2 and α-ScS_2, respectively. Similarly, S23b, S23d and S23f present the density of states for T-ScS_2, Hc-ScS_2 and α-ScS_2, where contributions from different atomic orbitals have been highlighted. All data has been normalised such that the highest occupied state (E_{Fermi}) is set to 0 eV.

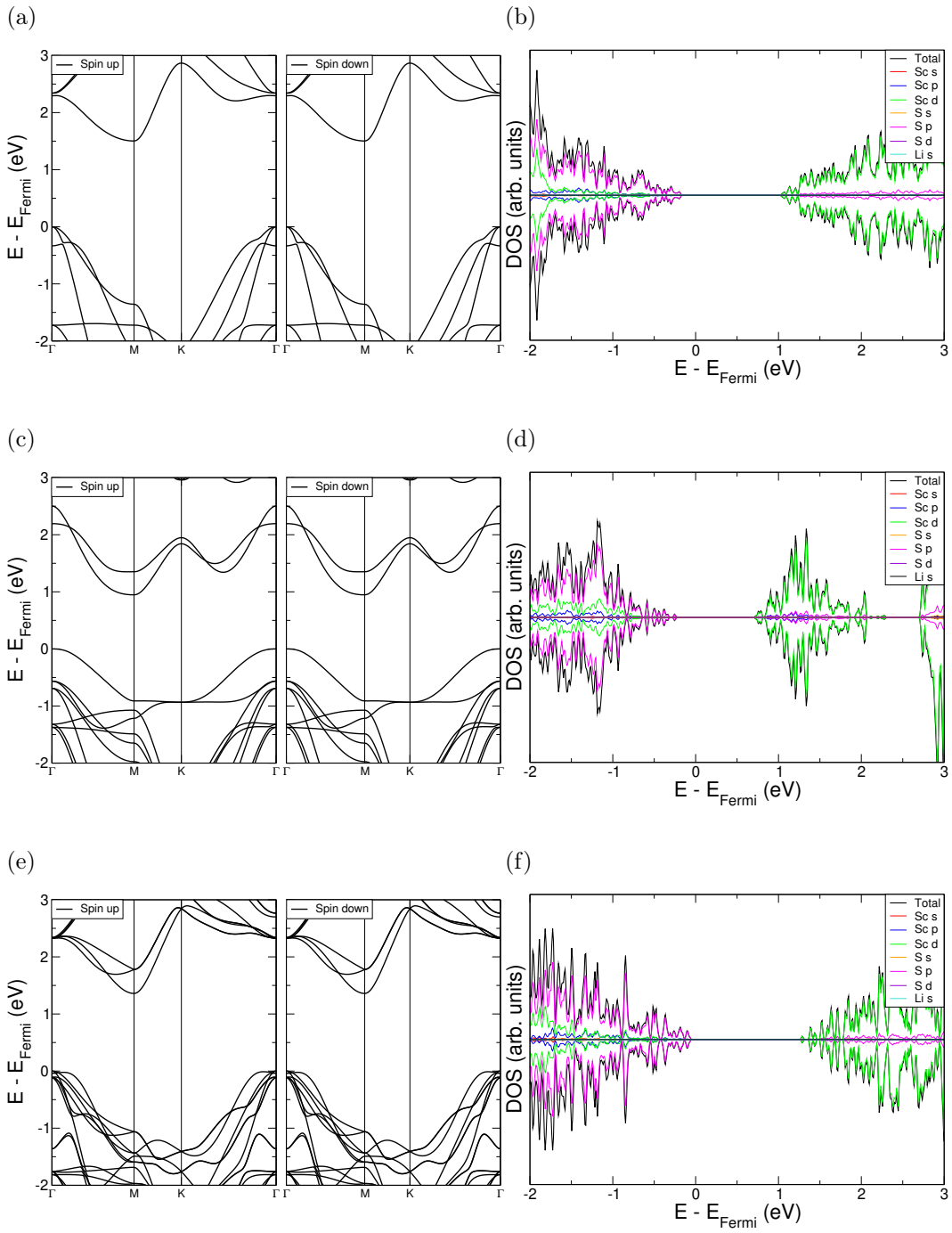

Figure S 24: Electronic band structures and orbital-decomposed density of states for lithium-intercalated phases of ScS_2. S24a, S24c and S24e present the band structures along high symmetry routes for T-$LiScS_2$, Hc-$LiScS_2$ and α-$LiScS_2$, respectively. Similarly, S24b, S24d and S24f present the density of states for T-$LiScS_2$, Hc-$LiScS_2$ and α-$LiScS_2$, where contributions from different atomic orbitals have been highlighted. All data has been normalised such that the highest occupied state (E_{Fermi}) is set to 0 eV.

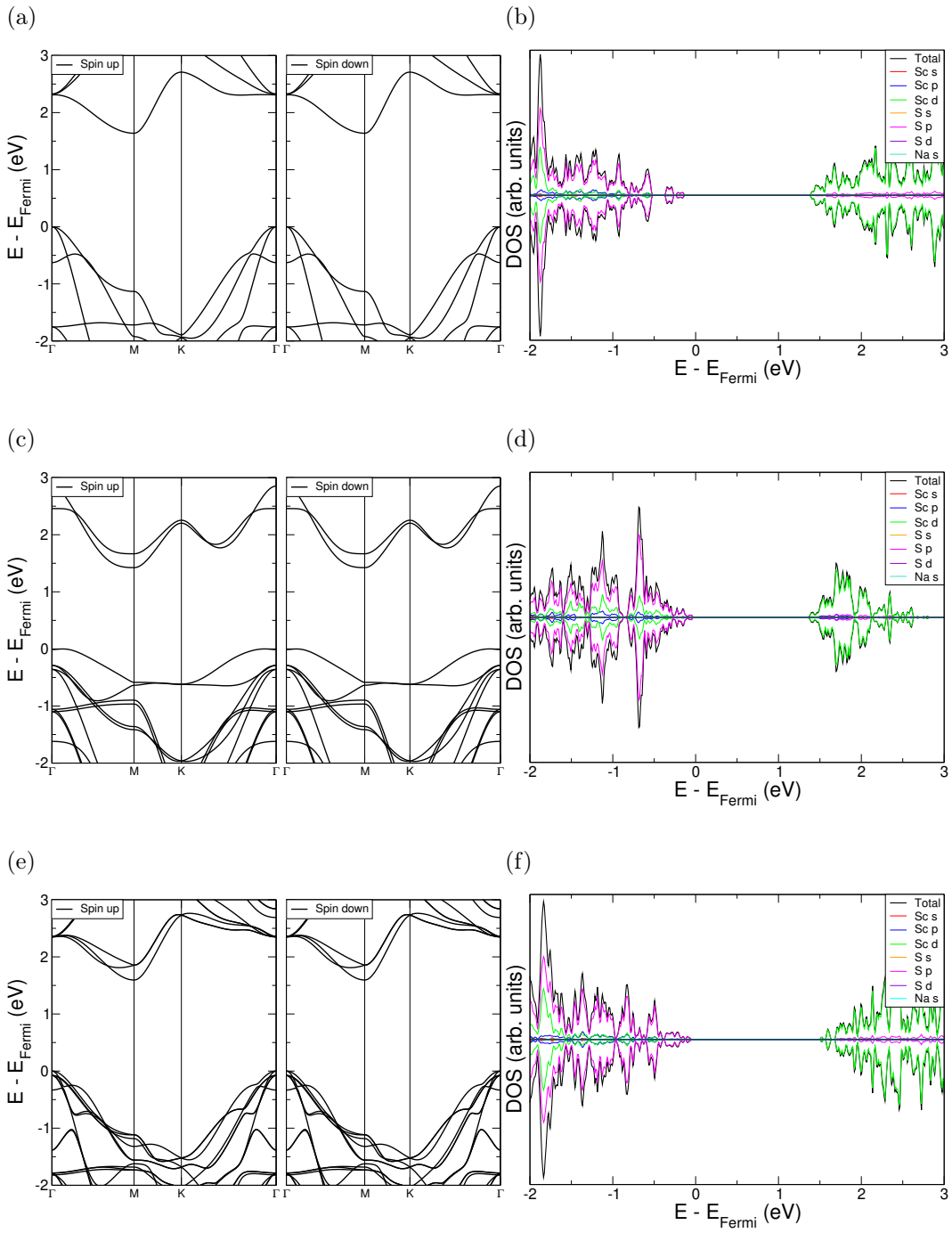

Figure S 25: Electronic band structures and orbital-decomposed density of states for sodium-intercalated phases of ScS_2. S25a, S25c and S25e present the band structures along high symmetry routes for T-$NaScS_2$, Hc-$NaScS_2$ and α-$NaScS_2$, respectively. Similarly, S25b, S25d and S25f present the density of states for T-$NaScS_2$, Hc-$NaScS_2$ and α-$NaScS_2$, where contributions from different atomic orbitals have been highlighted. All data has been normalised such that the highest occupied state (E_{Fermi}) is set to 0 eV.

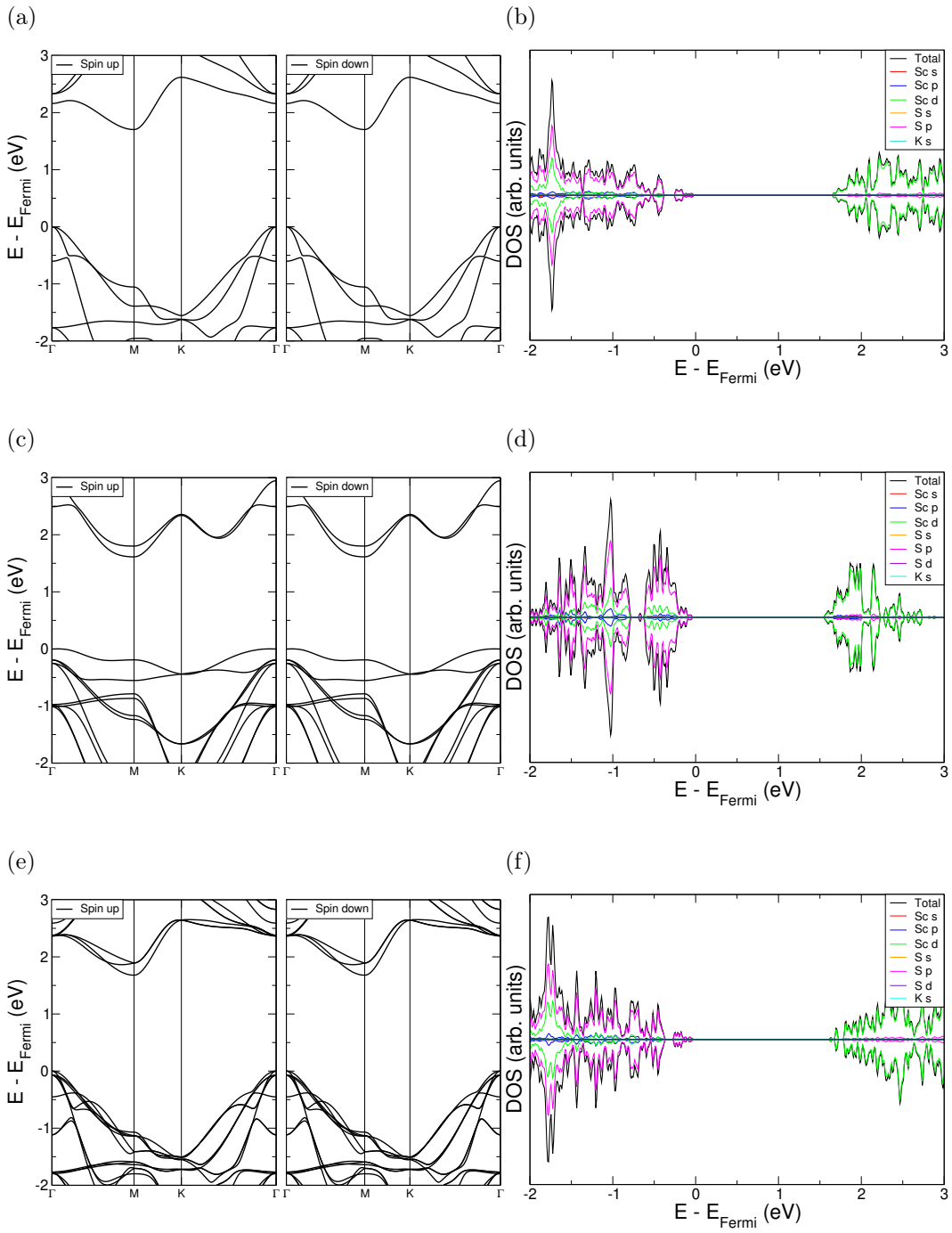

Figure S 26: Electronic band structures and orbital-decomposed density of states for potassium-intercalated phases of ScS_2. S26a, S26c and S26e present the band structures along high symmetry routes for T-$KScS_2$, Hc-$KScS_2$ and α-$KScS_2$, respectively. Similarly, S26b, S26d and S26f present the density of states for T-$KScS_2$, Hc-$KScS_2$ and α-$KScS_2$, where contributions from different atomic orbitals have been highlighted. All data has been normalised such that the highest occupied state (E_{Fermi}) is set to 0 eV.

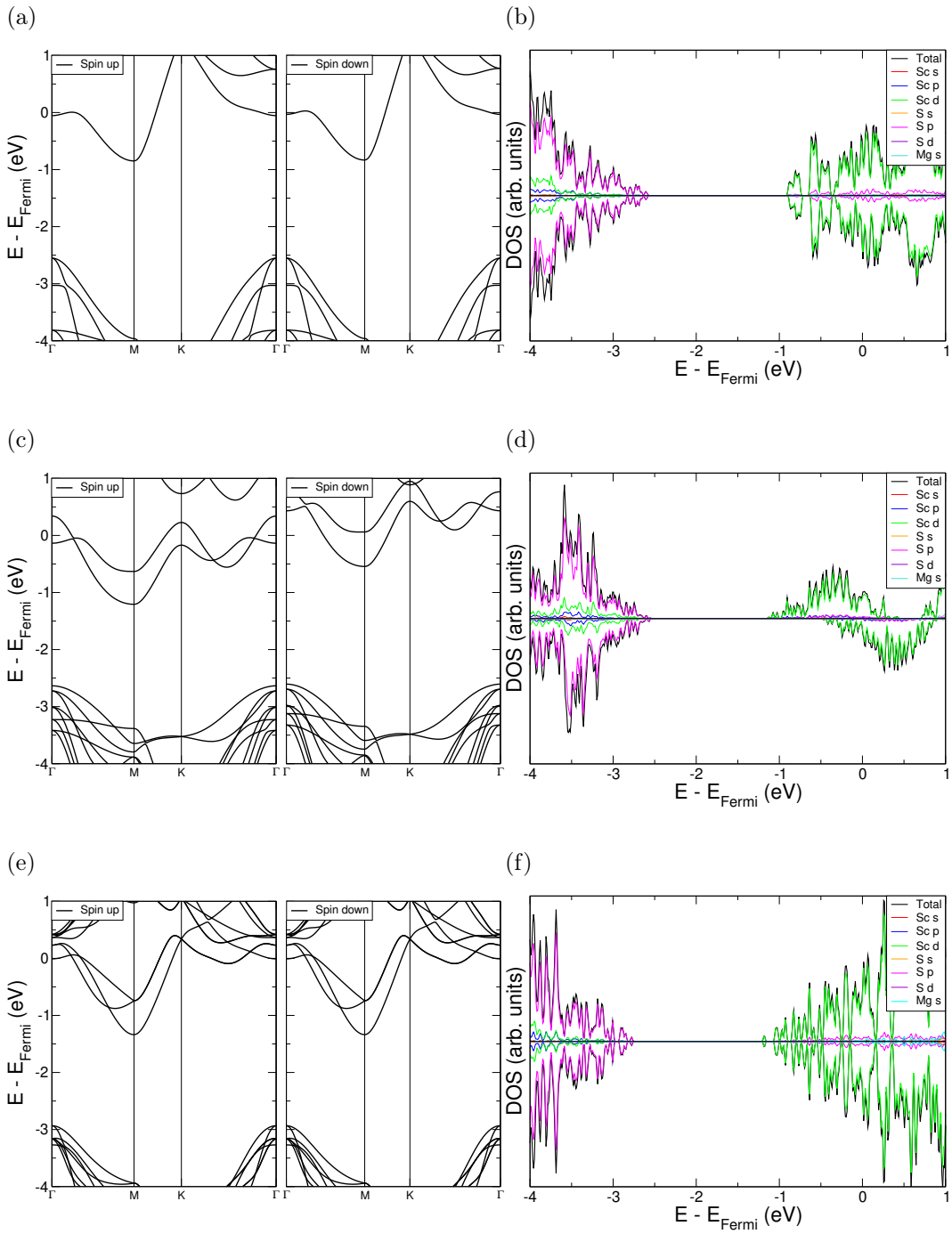

Figure S 27: Electronic band structures and orbital-decomposed density of states for magnesium-intercalated phases of ScS_2. S27a, S27c and S27e present the band structures along high symmetry routes for T-$MgScS_2$, Hc-$MgScS_2$ and α-$MgScS_2$, respectively. Similarly, S27b, S27d and S27f present the density of states for T-$MgScS_2$, Hc-$MgScS_2$ and α-$MgScS_2$, where contributions from different atomic orbitals have been highlighted. All data has been normalised such that the highest occupied state (E_{Fermi}) is set to 0 eV.

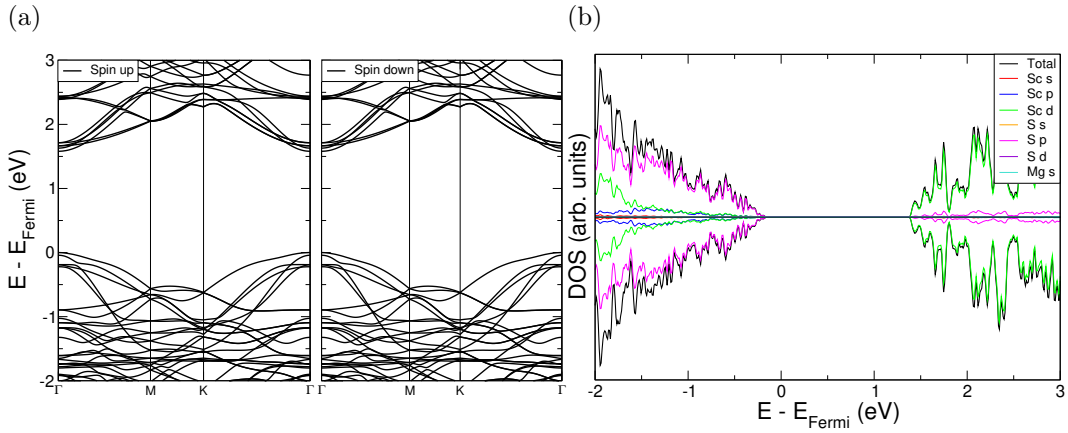

Figure S 28: Electronic band structure (a) and orbital-decomposed density of states (b) for T-ScS_2 intercalated with magnesium to $Mg_{0.5}ScS_2$.

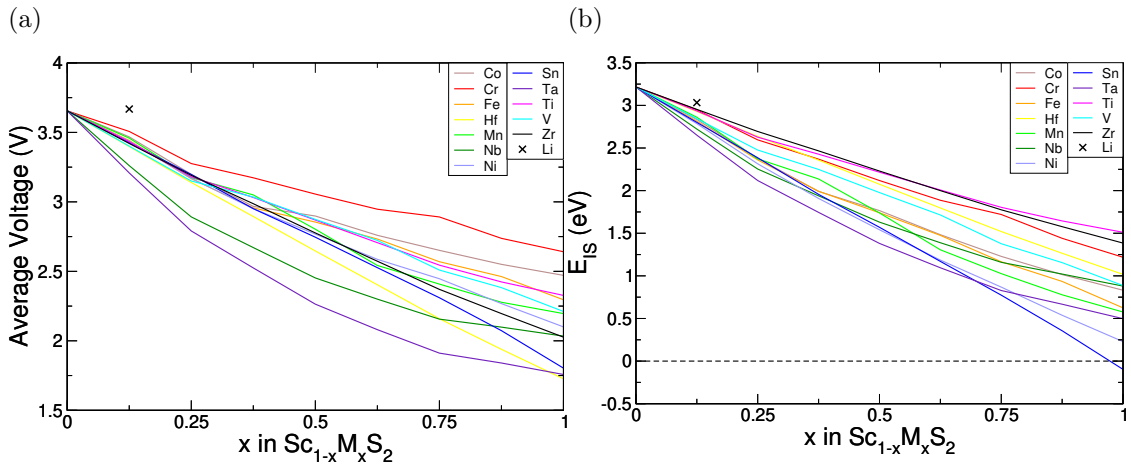

Figure S 29: Energetic results for metal mixing in T-ScS_2. S29a gives the average voltage for various metal mixing, calculated by taking the difference between the fully intercalated ($LiSc_{1-x}M_xS_2$) and pristine structures ($Sc_{1-x}M_xS_2$), and S29b gives the obtained values of E_{IS}.

XII. METAL MIXING

In Figure S29a, we show the variation in voltage as scandium is substituted for different metals. For each of the transition metals, it is clear to see a reduction in the intercalation potential as the proportion of scandium is reduced. The exception to this is demonstrated with lithium where, for a mixing concentration of x = 0.125, the average voltage is increased past the 3.655 V of ScS_2 to 3.668 V. The values of E_{IS} (at full lithium intercalation) for transition metal mixing demonstrate a similar trend, as shown in Figure S29b.

With changing metal composition, one might expect that the resulting values of voltage and E_{IS} would lie on a straight line connecting the respective values at x = 0 and x = 1. However, there is a varying amount of deviation from this expected linear trend for different metal species mixed. For example, the voltage and E_{IS} values for Hf (yellow), Sn (dark blue), and Zr (black) appear to follow very closely to a linear trend, whereas the trends of the other metals considered are much more convex. The convex shape is highlighted best with Ta (purple data), where there is a clear deviation from the straight line that would

connect the ScS_2 and TaS_2 limits.

---

* cjp225@exeter.ac.uk

† S.P.Hepplestone@exeter.ac.uk

[1] H. Katzke, P. Tolédano and W. Depmeier, *Physical Review B - Condensed Matter and Materials Physics*, 2004, **69**, 1–8.

[2] J. Ribeiro-Soares, R. M. Almeida, E. B. Barros, P. T. Araujo, M. S. Dresselhaus, L. G. Cançado and A. Jorio, *Physical Review B*, 2014, **90**, 115438.

[3] M. van Dijk and C. Plug, *Materials Research Bulletin*, 1980, **15**, 103–106.

[4] L. Havlák, J. Fábry, M. Henriques and M. Dušek, *Acta Crystallographica Section C Structural Chemistry*, 2015, **71**, 623–630.

[5] A. N. Enyashin and G. Seifert, *Computational and Theoretical Chemistry*, 2012, **999**, 13–20.

[6] Z. Liu, H. Deng and P. P. Mukherjee, *ACS Applied Materials and Interfaces*, 2015, **7**, 4000–4009.

[7] P. Gao, L. Wang, Y. Y. Zhang, Y. Huang, L. Liao, P. Sutter, K. Liu, D. Yu and E. G. Wang, *Nano Letters*, 2016, **16**, 5582–5588.

[8] S. Fan, X. Zou, H. Du, L. Gan, C. Xu, W. Lv, Y. B. He, Q. H. Yang, F. Kang and J. Li, *Journal of Physical Chemistry C*, 2017, **121**, 13599–13605.

[9] Z. Lu, S. Carr, D. T. Larson and E. Kaxiras, *Physical Review B*, 2020, **102**, 125424.

[10] G. Henkelman, B. P. Uberuaga and H. Jónsson, *Journal of Chemical Physics*, 2000, **113**, 9901–9904.

[11] G. Henkelman and H. Jónsson, *Journal of Chemical Physics*, 2000, **113**, 9978–9985.

[12] M. Woodcox, R. Shepard and M. Smeu, *Journal of Power Sources*, 2021, **516**, 230620.

[13] F. Mouhat and F.-X. Coudert, *Physical Review B*, 2014, **90**, 224104.

[14] C. J. Pickard and R. J. Needs, *Journal of Physics: Condensed Matter*, 2011, **23**, 053201.

[15] Y. Wang, J. Lv, L. Zhu and Y. Ma, *Computer Physics Communications*, 2012, **183**, 2063–2070.

[16] Q. Tong, J. Lv, P. Gao and Y. Wang, *Chinese Physics B*, 2019, **28**, 106105.

[17] T. Yamashita, S. Kanehira, N. Sato, H. Kino, K. Terayama, H. Sawahata, T. Sato, F. Utsuno, K. Tsuda, T. Miyake and T. Oguchi, *Science and Technology of Advanced Materials: Methods*, 2021, **1**, 87–97.

[18] W. Tipton and R. G. Hennig, 2014.

[19] A. Jain, S. P. Ong, G. Hautier, W. Chen, W. D. Richards, S. Dacek, S. Cholia, D. Gunter, D. Skinner, G. Ceder and K. A. Persson, *APL Materials*, 2013, **1**, 011002.

[20] D. Tristant, P. Puech and I. C. Gerber, *Physical Chemistry Chemical Physics*, 2015, **17**, 30045–30051.